REPUBLIC OF TÜRKİYE

YILDIZ TECHNICAL UNIVERSITY

GRADUATE SCHOOL OF SCIENCE AND ENGINEERING

INVESTIGATING THE OPTIMISATION OF THE FLUID FLOW DISTRIBUTION WITHIN A HIGH VOLTAGE BATTERY THERMAL CONDITIONING PLATE

Altan ÖZGÜR

MASTER OF SCIENCE THESIS

Department of Mechanical Engineering

Program of Heat and Process

Supervisor

Assoc. Prof. Dr. Zafer GEMİCİ

December, 2024

REPUBLIC OF TÜRKİYE

YILDIZ TECHNICAL UNIVERSITY

GRADUATE SCHOOL OF SCIENCE AND ENGINEERING

INVESTIGATING THE OPTIMISATION OF THE FLUID FLOW DISTRIBUTION WITHIN A HIGH VOLTAGE BATTERY THERMAL CONDITIONING PLATE

A thesis submitted by Altan ÖZGÜR in partial fulfillment of the requirements for the degree of **MASTER OF SCIENCE THESIS** is approved by the committee on 17.12.2024 in Department of Mechanical Engineering, Program of Heat and Process

Assoc. Prof. Dr. Zafer GEMİCİ
Yildiz Technical University
Supervisor

Approved By the Examining Committee

Assoc. Prof. Dr. Zafer GEMİCİ, Supervisor
Yildiz Technical University _____

Prof. Dr. Hakan DEMİR, Member
Yildiz Technical University _____

Prof. Dr. Aliihsan KOCA, Member
İstanbul Technical University _____

I hereby declare that I have obtained the required legal permissions during data collection and exploitation procedures, that I have made the in-text citations and cited the references properly, that I haven't falsified and/or fabricated research data and results of the study and that I have abided by the principles of the scientific research and ethics during my Thesis Study under the title of "Investigating The Optimisation Of The Fluid Flow Distribution Within A High Voltage Battery Thermal Conditioning Plate" supervised by my supervisor, Assoc. Prof. Dr. Zafer GEMİCİ. In the case of a discovery of false statement, I am to acknowledge any legal consequence.

Altan ÖZGÜR

Dedicated to my family

Mom and Dad

ACKNOWLEDGEMENTS

I extend my sincere gratitude to my esteemed thesis advisor, Assoc Prof. Dr. Zafer GEMİCİ, whose unwavering support and profound knowledge have been invaluable throughout my thesis endeavor.

I am deeply grateful to my cherished friends, Kamil Olszewski, Matthew Green, Mehaul Goswami, Christopher Elder, Mustafa Özçelik and Adam Mills for their steadfast encouragement and support throughout the course of my thesis research.

I wish to express my heartfelt appreciation to my parents, Tunca ÖZGÜR and Kenan ÖZGÜR whose continuous encouragement and support have been instrumental throughout my academic journey.

Altan ÖZGÜR

TABLE OF CONTENTS

LIST OF SYMBOLS vii
LIST OF ABBREVIATIONS ix
LIST OF FIGURES x
LIST OF TABLES xiiiii
ABSTRACT xiv
ÖZET xvii
1 INTRODUCTION 1
2 LITERATURE RESEARCH 3
2.1 Introduction to Literature Research Study 3
2.1.1 Heat Dissipation 3
2.1.2 Flow Distribution 6
2.1.3 Cooling Methods 8
3 INVESTIGATED CASE 10
3.1 Coolant flow distribution inside a cooling plate 10
4 THEORETICAL FRAMEWORK OF THE MODEL 13
4.1 Introduction to the Model 13
4.1.1 Governing Equations 13
4.1.2 k-ε Turbulance Model 14
4.1.3 Bouyancy Flows 16
4.1.4 Heat Transfer Mechanisms 17
4.1.5 Wall Functions 20
5 MODEL DEVELOPMENT 22
5.1 Study Case 22
5.2 Long Cooling Plate Flow Analysis Results 24
5.3 Short Cooling Plate Flow Analysis Results 26
5.4 Thermal Load Calculation 28
5.5 Boundary Conditions 30
5.6 Calculation of the Thermal Loads and Fluid Mass Flow 30

5.7 Thermal Conductance Calculation 31
5.8 Finite Element CFD Model Build 31
5.8.1 Thermal Assessment CFD Model 31
5.8.2 Flow Optimisation CFD Model 33
5.8.3 Prism Layer Settings 34
5.9 Pre Optimisation Results 36
5.10 Pre Optimisation Thermal Status 36
5.11 Reynolds Number Investigation 41
5.12 Initial Optimisation Results 44
5.13 Supplementary Flow Optimisation 46
5.14 Supplementary Optimisation Thermal Results 48
6 MODEL VALIDATION **50**
6.1 Validation Method 50
6.2 Execution of the Model Correlation Tests 52
6.3 Uncertainty Analysis 57
7 CONCLUSION **59**
REFERENCES **61**
PUBLICATIONS FROM THE THESIS **62**

LIST OF SYMBOLS

g	Acceleration due to gravity
A	Area
kg	Conduction heat transfer coefficient
°C	Degrees Celcius
°K	Degrees Kelvin
Δ	Delta
ρ	Density
DCIR	Direct current internal resistance
μ	Dynamic viscousity
Q	Heat Flow
h	Height
h	Hours
Dh	Hydraulic diameter
J	Joule
kg	Kilogram
L	Length
L	Litre
Ym	Magnitude of expansion dissipation
V̇	Mass Flow
M	Metre
mAh	Mili amper hour
mOhm	Mili ohm
m	Minutes
Nu	Nusselt Number
Ω	Ohm
Pa	Pascal
π	Pi constant
xi x-y-z	Position Tensors

P	Power
Pr	Prandlt Number
P	Pressure
Re	Reynolds Number
s	Seconds
Cp	Specific Heat
V	Speed
σ	Stefan-Boltzman constant
T	Temperature
t	Time, Duration
u	Velocity
V	Voltage
W	Watt

LIST OF ABBREVIATIONS

3D	3 Dimensional
ARC	Accelerating Rate Calorimeter
BEV	Battery Electric Vehicle
BEV	Battery Electric Vehicle
BTMS	Battery Thermal Management System
CH#	Channel number
C	Charge Rate
COP	Coefficient of Performance
CFD	Computational Fluid Dynamics
C	Coulomb
EV	Electric/Electrified Vehicle
HVAC	Heating Ventilating Air Conditioning
HV	High Voltage
DH	Hydraulic Diameter
LIB	Lithium Ion Battery
Max	Maximum
Min	Minimum
Min	Minutes
NCM	Nickel Cobalt Manganese
SOC	State Of Charge

LIST OF FIGURES

Figure 2.1 Test mechanism used for battery specific heat measurement.....**4**

Figure 2.2 Generated heat based on specific heat capacities on time domain. Including the relative error.....**4**

Figure 2.3 Battery internal resistance in different at 25˚C to 55˚C temperatures on SOC domain.....**5**

Figure 2.4 Comparing calculated and tested battery heat generation values for T0:25◦C with 1C discharge rate.....**5**

Figure 2.5 Change of generated heat under different operating conditions on time domain.....**5**

Figure 2.6 The 4 geometries proposed for disturibing the coolant fluid.....**6**

Figure 2.7 CFD flow analysis results for coolant fluid speed in the 4 proposed geometries.....**6**

Figure 2.8 Comparison of the proposed 4 geometries for the average fluid flow velocities on each channel.....**7**

Figure 2.9 CFD analysis result showing the effects of having different numbers of dimples/deflectors over fluids mass flow and velocity.....**7**

Figure 2.10 Classification of the cooling techniques.....**8**

Figure 2.11 Refrigerant-based indirect cooling arrangement **9**

Figure 3.1 Single battery stack module.....**10**

Figure 3.2 Coolant plate.....**11**

Figure 3.3 Isometric section view of the cooling plate.....**11**

Figure 3.4 Flow analysis before optimization.....**12**

Figure 5.1 Battery pack cooling system layout.....**22**

Figure 5.2 Isometric section view of the cooling plate showing internal channels **23**

Figure 5.3 Single battery stack module.....**23**

Figure 5.4 Coolant plate.....**23**

Figure 5.5 Long cooling plate pressure drop analysis result **24**

Figure 5.6 Long cooling plate fluid velocity analysis result.....**24**

Figure 5.7 Long cooling plate end tank and coolant flow distribution from inlet spigot to channels.....**25**

Figure 5.8 Long cooling plate channels fluid mass flow deviation from average CFD analysis result **25**

Figure 5.9 Short cooling plate pressure drop analysis result **26**

Figure 5.10 Short cooling plate fluid velocity analysis result **26**

Figure 5.11 Short cooling plate end tank and coolant flow distribution from inlet spigot to channels **27**

Figure 5.12 Short cooling plate channels fluid mass flow deviation from average CFD Analysis Result **27**

Figure 5.13 Battery cell stack Mesh view **32**

Figure 5.14 Thermal Model measurement points **33**

Figure 5.15 Cooling plate coolant fluid volume mesh model **33**

Figure 5.16 Prism layer comparison on wallfluid boundary **34**

Figure 5.17 Thermal analysis legend before flow optimisation and min max temperatures taken from extreme points of the cells **36**

Figure 5.18 Inlet manifold with deflector inside **37**

Figure 5.19 Deflector in front of cooling plate **37**

Figure 5.20 Channel entry point distances to spigot reference point (straight distance) **38**

Figure 5.21 Deflector entrance and deflector exit geometries **38**

Figure 5.22 Cooling plate internal channels and fluid flow routes **39**

Figure 5.23 Bend loss coefficients for a pipe **40**

Figure 5.24 Moody friction diagram **40**

Figure 5.25 Coolant flow stream channels **41**

Figure 5.26 Notable deflector design iterations **43**

Figure 5.27 Post optimisation cooling plate pressure drop status **44**

Figure 5.28 Post optimisation channel mass flow deviations **44**

Figure 5.29 Post initial optimisation cell minimum and maximum cell temperature values **45**

Figure 5.30 Top and bottom cells lacking contact surface to cooling plate **46**

Figure 5.31 Deflector Iteration 15 Section view **46**

Figure 5.32 Deflector Iteration 15 massflow distribution vs target **47**

Figure 5.33 Deflector Iteration 15 pressure drop **48**

Figure 5.34 Deflector Iteration 15 thermal results **48**

Figure 6.1 3D printed Venturi tube in the middle of the cooling plate **50**

Figure 6.2 CFD Model of the 3D printed Venturi tube for correlation **50**

Figure 6.3 Model correlation test rig **51**

Figure 6.4 Original plate geometry model delta pressure measuring test rig **51**

Figure 6.5 Venturi plate geometry model delta pressure measuring test rig **52**

Figure 6.6 Fluid bottle height is lowered to reduce the pressure required due to the height difference on the return line **52**

Figure 6.7 Example static pressure measurement from plate outlet an inlet using water as liquid **54**

Figure 6.8 Example static pressure measurement from plate outlet an inlet using ethanol coolant mixture as liquid **54**

Figure 6.9 Example static pressure measurement from 5mm and 10mm ID tubes using water as liquid **55**

Figure 6.10 Example static pressure measurement from 5mm and 10mm ID tubes using ethanol water mixture as liquid **55**

Figure 6.11 Ruler and graph paper alignment.....**55**

Figure 7.1 Top and Bottom cells' missing contact area with cooling plate.....**59**

LIST OF TABLES

Table 5.1 Boundary conditions **24**

Table 5.2 Long cooling plate channels fluid mass flow deviation from average CFD Analysis Resultxample table **26**

Table 5.3 Short cooling plate channels fluid mass flow deviation from average CFD analysis Result **28**

Table 5.4 Physical properties **29**

Table 5.5 HV Battery cell specification **29**

Table 5.6 Design boundary conditions and targets **30**

Table 5.7 Mesh cell, face and vertice numbers for the CAE model components **32**

Table 5.8 Mesh Parameters **34**

Table 5.9 Prism layer 6 & 10 comparison CFD flow results for Base (No deflector) design **35**

Table 5.10 Prism layer 6 & 10 comparison CFD flow results for (No:9 deflector) design **35**

Table 5.11 Reynolds numbers calculated for each stream section channel **42**

Table 5.12 Pre and post initial optimisation flow deviation comparison **45**

Table 5.13 Reynolds numbers calculated for each stream section channel on supplemetary optimisation geometry **47**

Table 5.14 Initial and supplementary optimisation thermal comparison **49**

Table 6.1 Comparison of CFD results with physical test measurements **56**

Table 7.1 Comparison of the engineering targets and optimisation results **60**

ABSTRACT

Investigating The Optimisation Of The Fluid Flow Distribution Within A High Voltage Battery Thermal Conditioning Plate

Altan ÖZGÜR

Department of Mechanical Engineering

Program of Heat and Process

Master of Science Thesis

Supervisor: Assoc. Prof. Dr. Zafer GEMİCİ

Electrified and fully electric vehicles are promising solution to create healthier and sustainable environment by reducing the unhealthy exhaust and greenhouse gases emitted into atmosphere by motor vehicles. Today Lithium-Ion batteries are considered to be the most feasible energy storage for EVs thanks to their advantages on cost, volumetric and gravimetric energy density, charging speed, power delivery and lifetime capabilities. On the other hand, the performance, lifetime and safety attributes of these type of battery cells are highly dependent to the operating and storage temperatures. Operating and storing lithium-ion batteries outside of their optimal range leads to reduced performance and increased aging over time. Therefore ensuring the batteries are kept in their optimal storage and operating temperature is a key element of the battery pack design targets. The energy storage and performance delivery capabilities of an HV battery pack is also limited by its weakest cell. In example faster aging cells in a pack will become bottle neck on storage and performance of the healthier cells of the pack. Therefore, cooling

system must not only be able to keep the cells within an optimal temperature range but also should be minimizing the temperature deviation among the battery cells to prevent significant aging gaps between the cells. On a fluid cooling systems this can be obtained by using well balanced cooling distribution, control systems using valves and sensors, software controlled charge and discharge operations and so on. In this thesis the optimization of the coolant flow distribution within an HV Battery cell pack cooling plate is investigated using CFD methods while adhering to the boundary conditions. Then the correlation of the CFD model is tested and confirmed with the measurements taken from test rigs using prototype parts.

Keywords: Flow Distribution, optimisation, coolant, cooling plate, computational fluid dynamics (CFD)

ÖZET

Yüksek Gerilim Bataryası Isıl Şartlandırma Plakasında İş Akışkanının Akış Dağılımının Optimizasyonu

Altan ÖZGÜR

Makine Mühendisliği Anabilim Dalı
Isı-Proses Programı
Yüksek Lisans Tezi

Danışman: Doç. Dr. Zafer GEMİCİ

Elektrikli ve tamamen elektrikli araçlar, motorlu araçlarca atmosfere salınan sağlıksız egzoz ve sera gazlarını azaltarak daha sağlıklı ve sürdürülebilir bir çevre yaratmak için umut vadeden bir çözüm sunmaktadırlar. Günümüzde Lityum iyon piller, maliyet, hacimsel ve kütlesel enerji yoğunluğu, şarj hızı, güç iletim kapasitesi ve kullanım ömrü niteliklerindeki avantajları sayesinde elektrikli araçlar icin en uygun enerji depolama yöntemi olarak kabul edilmektedirler. Bununla beraber, Lityum iyon pil hücrelerinin güç iletim, kullanım ömrü ve güvenlik özellikleri, çalışma ve depolama sıcaklıklarına büyük ölçüde bağlıdır. Lityum iyon pillerin optimum aralıklarının dışında çalıştırılması ve depolanması, zamanla performanslarının düşmesine ve yıpranmanın artmasına neden olur. Bu nedenle pillerin optimum depolama ve çalışma sıcaklığında tutulmasını sağlamak, pil paketi tasarım hedeflerinin temel unsurudur. Bir yüksek gerilim pil paketinin enerji depolama ve performans kapasite nitelikleri en zayıf hücresinin kapasitesi ile sınırlıdır. Örneğin, bir pil paketi icinde hızlı yıpranan hücreler, paketin sağlıklı hücrelerinin enerji depolama ve güç iletim niteliklerinde darboğaz yaratmaktadırlar. Bu nedenle pil paketi soğutma sistemi pil hücrelerini yalnızca

optimum sıcaklık aralığında tutmakla kalmamalı aynı zamanda pil hücreleri arasında önemli yıpranma farklarının oluşmasını önlemek amacıyla pil hücreleri arasındaki sıcaklık farklarını da en aza indirmelidir. Bir soğutma sisteminde bu, dengelenmiş soğutma dağılımı, valf ve sensörler ile çalışan kontrol sistemleri, şarj ve deşarj yüklerini yazilim ile kontrol etmek gibi yöntemlerle saglanabilir. Bu tezde, sınır koşullarına bağlı kalarak bir pil hücre paketi soğutma plakası içindeki soğutucu akış dağılımının optimizasyonu HAD yöntemleri kullanılarak incelenmiştir. HAD modelinin korelasyonu ise prototip parça ve test düzeneklerinden alınan ölçümlerle doğrulanmıştır.

Anahtar Kelimeler: Akış dağılımı, optimizasyon, soğutma sıvısı, soğutma plakası, hesaplamalı akışkanlar dinamiği (HAD)

1
INTRODUCTION

Electrified vehicles are promising solution for a low or no exhaust gas emitting transportation and green environment in areas they are used. One of the major challenges for EVs is to build an energy storage system that provides long range, has a long lifetime, capable of fast charging and that delivers the stored energy efficiently with high performance. Today Lithium-Ion batteries are considered to be the most feasible power source for EVs due to their advantages such as, cost, energy density, charging speed, power delivery and lifetime. The performance, lifetime and safety attributes are highly dependant on operating and storage temperatures. Therefore, battery thermal management systems are designed to prevent the batteries from adverse effects of extreme cold and hot temperatures.

Cell-to-cell variations, such as voltage, state of charge, capacity and internal resistance are can reduce the lifetime and performance of Li Ion cells. Operating and storing lithium-ion batteries outside of their optimal operating temperatures leads to reduced performance and increased aging in the long and short terms. In most applications HV battery cells are designed to be stacked together for the lifetime of the HV battery and the performance is limited by the weakest cell. One of the key objectives of an HV battery cooling system is to minimize the temperature deviation among the battery cells whilst keeping the temperature within the safe working temperature range. Therefore the cooling system needs to provide homogenous cooling performance by distributing the coolant or the refrigerant evenly over the cells, preventing long lasting temperature gaps between the cells. Most HV batteries are using closed circuit cooling system with aluminium cooling plates in touch condition with HV battery cells and water-glycol mixture flowing throught the plate channels as the thermal conditioning fluid. The Thermal cooling/heating performance and flow distribution of the fluid is virtually assessed

using CFD, optimized by changing adding or removing geometries and tested in physical rigs.

Today the automotive industry is facing a very big competition in the race of delivering electrified or fully electric vehicles into the market. This is making the pace of product development very critical.

On the other hand, automotive industry is facing a prejudice from the consumer side against electrifiation. One of the prominent doubt of the consumer is the lifetime of the HV battery and the cost to repair or replace. Therefore elongating the usable lifetime of an EV battery and minimizing the repair cost and avoiding full replacements is becoming crucial.

Temperature optimization and cell balancing is key design actions in achieveing robust and reliable battery.

In this thesis we will be working on improving the cooling distirbution over a stack of battery cells to achieve evenly distributet cooling effect, so that minimize the aging gaps between the cells.

We will be using CFD to calculate the thermal loads and coolant flow deviations.

Then we will be bringing design solutions whilst staying within the boundary condiotons and enginering targets. We will be using iterative and parametised designs and analyisis to reach the solution faster and cost efficiently.

- This thesis consists of several sections.
- The very first section is the introduction to the thesis.
- The Second section is literature research on coolant flow optimization studies.
- The Third section is the details of the case study.
- In the fourth section the theoretical framework behind the finite element methods and computational fluid dynamics can be found.
- The fifth section consists of the model development and optimization.
- The Sixth part is the validation of the models and the results.
- And the 7th part is the conclusion and lessons learned.

2
LITERATURE RESEARCH

2.1 Introduction to Literature Research Study

When we look into the literature, we see that many research studies are carried over HV battery thermal heat dissipation and thermal conditioning. Especially with the developments on the CFD tool capabilities and increase on the computational power many different methots and practices have arised within the field. On heat dissipation side we have reviewed couple of resaerch studies investigating the heat dissipation of the particular battery cell used in our studies. Hence if we take the main part of our study which is the coolant flow optimisation, it is hard to find research studies that match with the particular problem we are trying to resolve. On the other hand, as the flow distribution is not an subject only on battery thermal conditioning, there are various research studies done on different applications, such as electronics and engine cooling systems. There are different types of cooling methods investigated and are also currently in use like, liquid cooling, air cooling and phase changing material cooling methods, in this section we will touch on these briefly.

2.1.1 Heat Dissipation

Lin C. et al. [1] have investigated the heat dissipation of a 21700 form factor NCM Li-Ion cell in their study. In their research the heat capacity, heat generation, internal resistance of an NMC type 21700 form factor Lithium-Ion cells under different ambient and operation temperatures, charge/discharge speeds, operation durations and SOC's have been investigated.

ARC (Accelerating Rate Calorimeter) method using a calorimeter has been used to measure battery cell specific heat capacity.

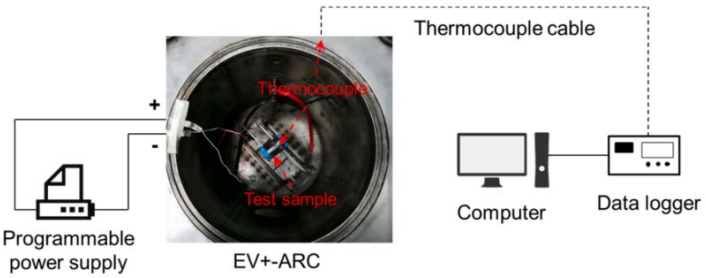


Figure 2.1 Test mechanism used for battery specific heat measurement

The law of conversation of the energy has been used to calcualte the specific heat capacities. The heat generated by thebattery cells has been measured using ARC method. The test mechanism can be seen in figure 2.1. The following graphs has been generated representing thermal properties and behaviour of NMC 21700 battery cell in different discharge rates and ambient&cell temperatures. It is observed that the heat generation is increasing with discharge rate and decreisng with temperature.

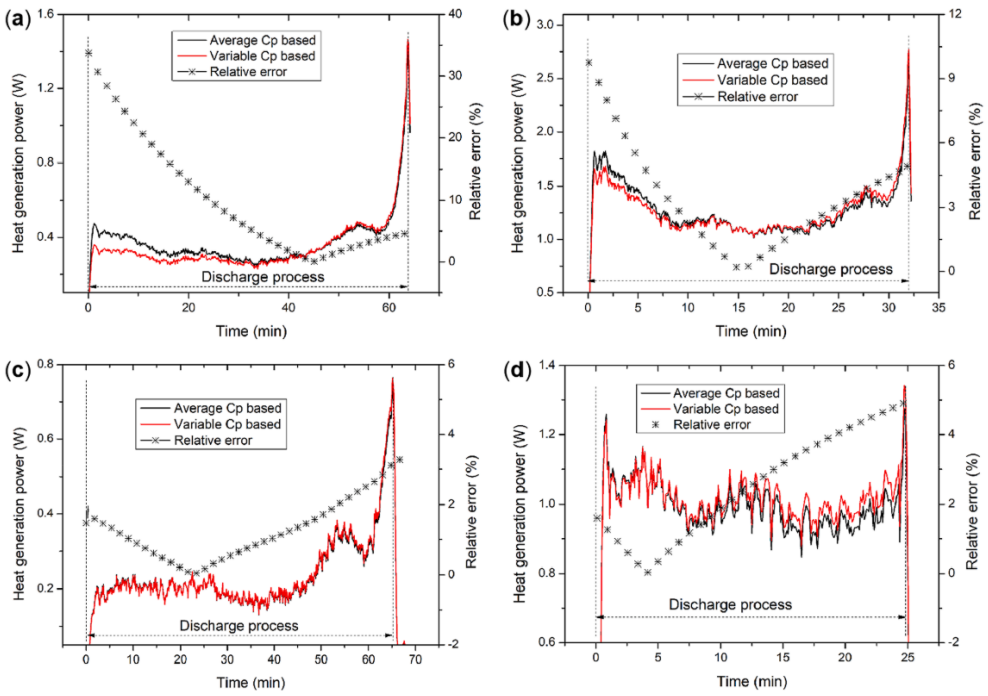


Figure 2.2 Generated heat based on specific heat capacities on time domain. Including the relative error. (a) T_0: 25˚C at 1C rate, (b) T_0: 25˚C at 2C rate, (c) T_0: 40˚C at 1C rate, (d) T_0 : 40˚C at 2C rate.

Figure 2.2 shows generated heat from the cells under different discharge conditions.

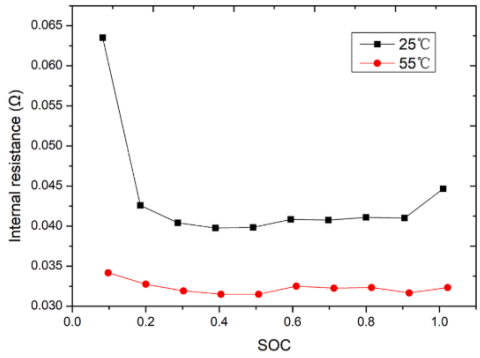


Figure 2.3 Battery internal resistance in different at 25˚C to 55˚C temperatures on SOC domain

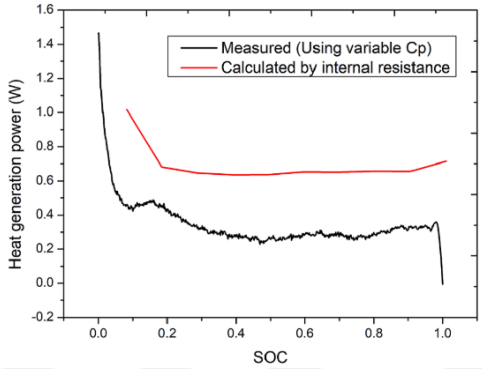


Figure 2.4 Comparing calculated and tested battery heat generation values for T_0:25˚C with 1C discharge rate

Figure 2.3 and Figure 2.4 show the internal resistance of the battery cell, the main source of heat generation, changes with SOC of the battery cell and cell temperature. It can be observed that the internal resistance is consistent until low SOC levels. But it suddenly peaks when it is close to full deplete. And the internal resistance of the battery cell is low close to limit hot temperatures.

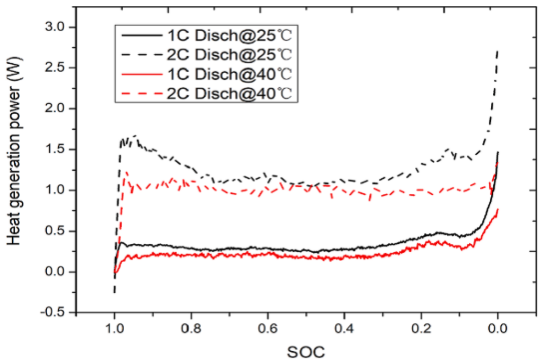


Figure 2.5 Change of generated heat under different operating conditions

Figure 2.5 shows how the amount of the generated heat is changing under different discharge rates and temperatures.

2.1.2 Flow Distribution

E. Vásquez-Alvarez et al. [2] have used CFD tools to evaluate the homogeneity of fluid flow distribution in the microchannels in their research. Four geometries shown in figure 2.6 were proposed and simulated in two and three dimensions to show that geometric details directly affect the distribution of velocity in the micro-heat exchanger channels. Similar to our optimization study different type of geometries have been evaluated to reduce the coolant mass flow deviation among the coolant flow channels. Results can be observed in figure 2.7.

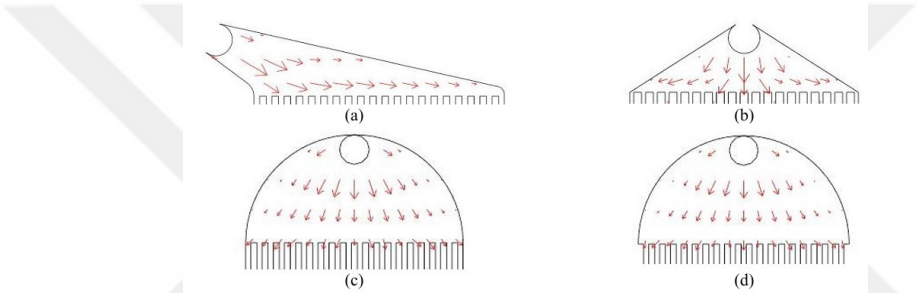


Figure 2.6 The 4 geometries proposed for distribing the coolant fluid

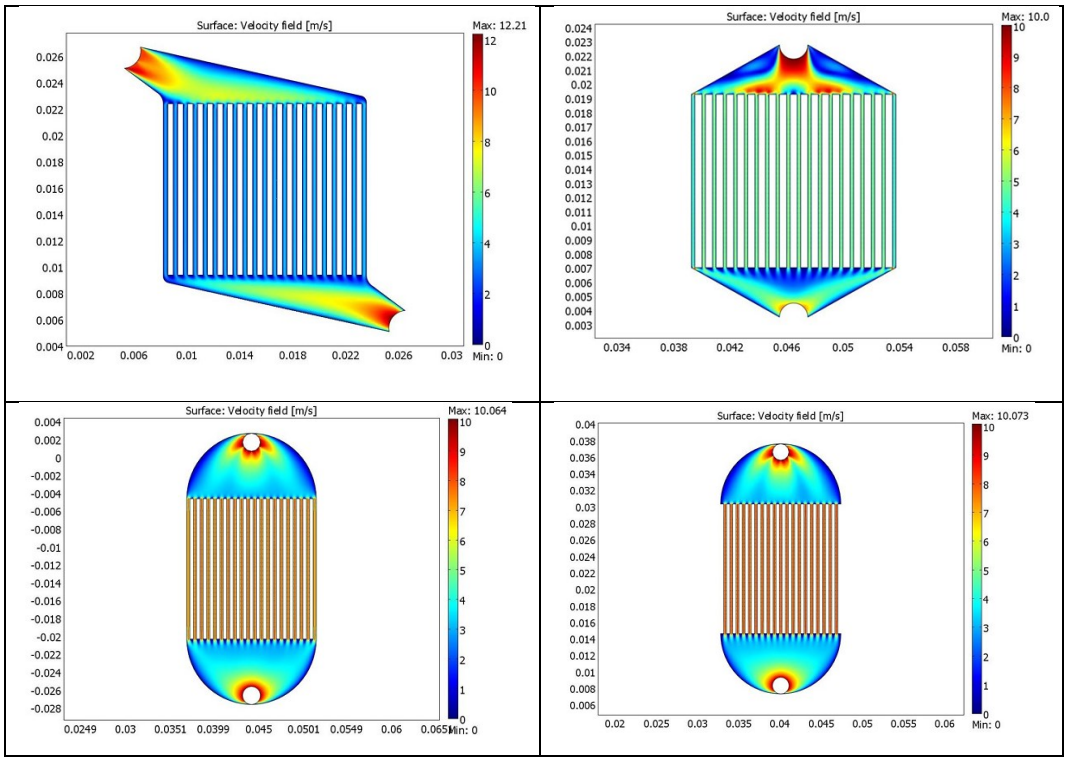


Figure 2.7 CFD flow analysis results for coolant fluid speed in the 4 proposed geometries

In another research carried by Zhao D. et al [3] reviewed different coolant deflector shapes within cooling plates to achieve homogeneous flow. However the problem they are approaching is slightly different, also the manufacturing method (stamped double layer cooling plate) allows wider modification on the cooling plate. The impact of different geometries to the flow on thir studies can be observed in figures 2.8 and 2.9.

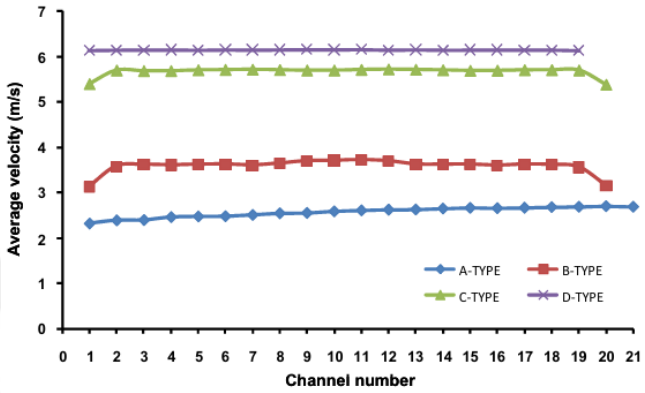
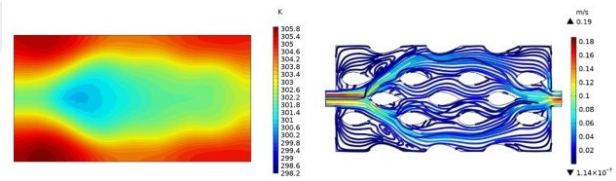
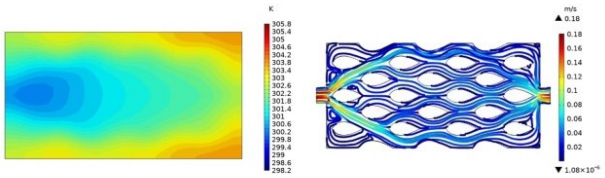


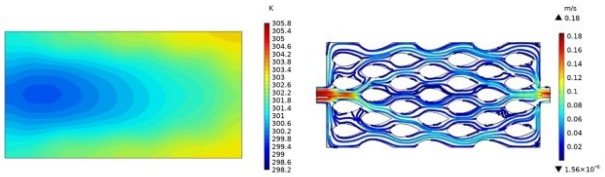
Figure 2.8 Comparison of the proposed 4 geometries for the average fluid flow velocities on each channel



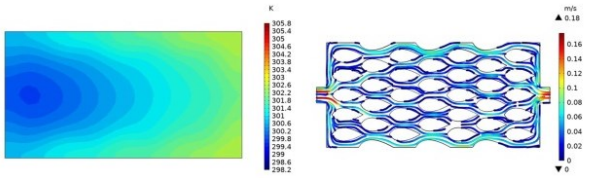
(a) 11 deflectors



(b) 18 deflectors



(c) 25 deflectors



(d) 32 deflectors

Figure 2.9 CFD analysis result showing the effects of having different numbers of dimples/deflectors to the over fluids mass flow and velocity

In our thesis we will be investigating how to guide coolant flow into the extruded aluminium coolant plate channels before it enters the channels.

2.1.3 Cooling Methods

Shaikh U. I. et al. [4] investigated different types of cooling methods used in different application of lithium ion batteries. In their research they split cooling systems based on their energy consumption in three main categories. Active, Passive and hybrid cooling.

Active cooling requires the most energy to power the cooling components, such as fans, pumps, or compressors to circulate or pressurize the coolant fluids. Passive cooling requires moderate energ. Hybrid cooling combines active and passive cooling methods, ie mixing phase change materials with air and liquids or even using it in heat pipes. Figure 2.10 is showing the hierarchy of different cooling techniques used for battery packs.

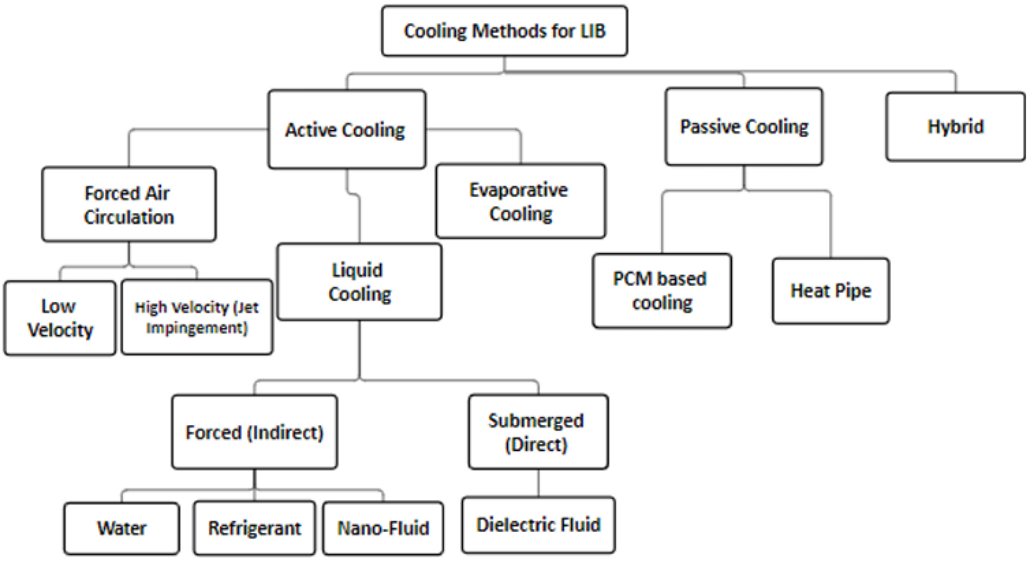


Figure 2.10 Classification of the cooling techniques

In our literature research we will touch only on the cooling type used in our investigation study which is indirect refrigerant-based cooling arrangement.

The research publication advises as following “in high power EV’s, refrigerant of the vehicle’s heating ventilation and air conditioning system (HVAC) is used as a cooling fluid (Figure 2.11). In direct refrigerant cooling the refrigerant is circulated through the cooling plate channel situated around the batteries. In indirect

refrigerant cooling the refrigerant is used to cool down another coolant (generally water + ethylene glycol) which in turn is circulated though the cold plate to absorb heat from battery pack. With the use of fins in the refrigerant heat exchanger, the temperature of the battery pack can be controlled under 35 °C in extreme surrounding temperature of 40°C and the 'ΔTmax' can be maintained well below 4 °C for typical road drive cycles."

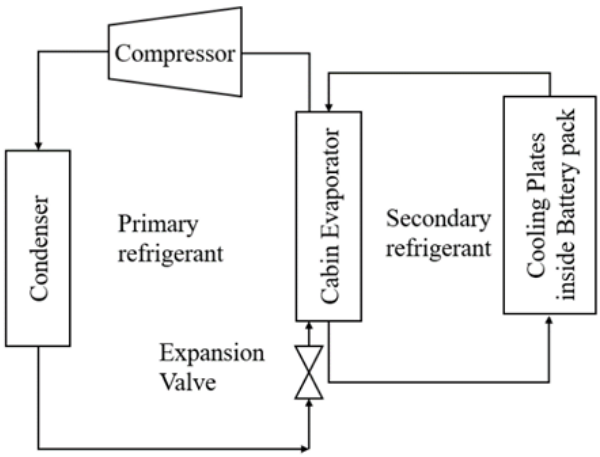


Figure 2.11 Refrigerant-based indirect cooling arrangement

3
INVESTGATED CASE

3.1 Coolant Flow Distribution Inside a Cooling Plate

As mentioned in the introduction section, a battery pack's performance is limited by its weakest cell. So it is required to ensure that the aging gap between the cells of a battery pack is not or it is widening at a minimum feasible pace throughout the life of the HV battery. Preventing temperature variation across the cells of a pack requires all cells to be kept within an optimal and uniform operating temperature.

We will be investigating the heat dissipation and the optimization of the coolant flow distribution within a HV battery cooling plate that had to have an off center coolant inlet and outlets, causing imbalance in coolant flow.

The HV battery stack module that we are going to study has 160 Serial 2 parallel configuration in one single stack. It is being thermally conditioned with 2 coolant plates. Figure 3.1 resembles the assembly of battery cells whilst Figure 3.2 shows the single cooling plate.

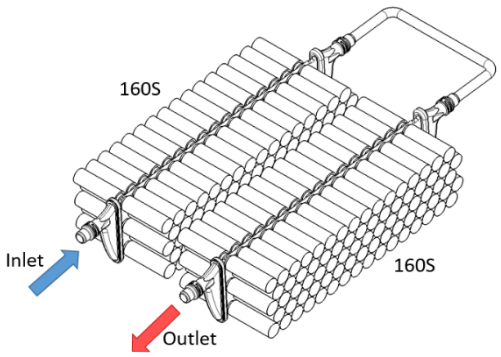


Figure 3.1 Single battery stack module

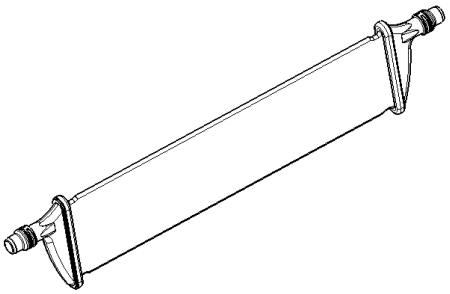


Figure 3.2 Coolant plate

The coolant plate has plastic manifolds at both ends. Due to package constraints in the design of the electric vehicle the inlet and outlet spigots had have to be off centric. Remaining package space is occupied by battery stack electronics control systems. The off centric inlet and outlet configuration is causing the coolant mass flow being distributed unevenly between the liquid channels within the cooling plate. This non-uniformity is causing uneven cooling effect to the battery cells and leading to early aging on the cells receiveing less heat discharge.

As a result, uneven aging and performance loss across the battery cells is occurring. Since the automotive HV battery cells are permanently connected to each other, the system can only be operated until the limits of the weakest cell are reached. Therefore, balancing procedures are the state-of-the-art solution to meet the challenge of cell-to-cell variations and increase the usable capacity or usage time. Objective is set to reach no more than 5% coolant flow deviation across the coolant plate channels, and less than 5˚C temperature gap on critical use case.

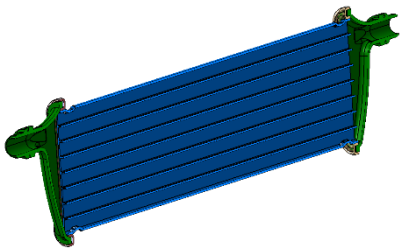


Figure 3.3 Isometric Section view of the cooling plate

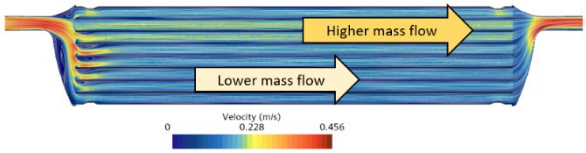


Figure 3.4 Flow Analysis before optimization

Figure 3.3 shows the internal 8 flow channels in the section view of the cooling plate. Figure 3.4 shows results of the initial flow analysis. The 2nd and 3rd channels (ordered from top) are getting higher coolant mass flow than the other, especially the furthest 8th channel.

4
THEORETICAL FRAMEWORK OF THE MODEL

4.1 Introduction to the Model

In this section, the theorems used during the creation of the numerical model and the numerical solver are introduced. Also the approaches used by the solver program will be briefly mentioned.

4.1.1 Governing Equations

The Siemens SimCenter Star CCM+ program that we use as a solver in this dissertation project solves the Navier-Stokes equations, that mathematically express momentum balance for Newtonian Fluids and make use of conservation of mass. Those will be briefly mentioned in this section.

In fluid mechanics Navier-Stokes equations show that the change on the momentum is equal to the sum of the pressure changes, and the friction losses caused by the viscous forces. Viscous forces are a result of intermolecular interactions and represent the resistance to flow of the fluid. In short, the Navier-Stokes Equations reflect the forces' dynamic equilibrium in each given fluid region.

Navier-Stokes equations, like the other equations used as solvers; are derived from mass, momentum and energy equations. These equations are expressed in various ways in many sources, but basically they are as following;

$$\frac{\partial \mathrm{p}}{\partial \mathrm{t}} + \frac{\partial \mathrm{p u_i}}{\partial \mathrm{x_i}} = 0 \tag{4.1}$$

$$\frac{\partial \rho \mathrm{u_i}}{\partial \mathrm{t}} + \frac{\partial \rho \mathrm{u_i u_j}}{\partial \mathrm{x_j}} = -\frac{\partial \mathrm{P}}{\partial \mathrm{x_i}} + \frac{\partial}{\partial \mathrm{x_j}}\left[\mu\left(\frac{\partial \mathrm{u_i}}{\partial \mathrm{x_j}} + \frac{\partial \mathrm{u_j}}{\partial \mathrm{x_i}}\right)\right] \tag{4.2}$$

$$\frac{\partial \rho \mathrm{T}}{\partial \mathrm{t}} + \frac{\partial \mathrm{p T u_j}}{\partial \mathrm{x_j}} = \frac{\partial}{\mathrm{c_p}\,\partial \mathrm{x_j}}\left(\mathrm{k}\frac{\partial \mathrm{T}}{\partial \mathrm{x_j}}\right) \tag{4.3}$$

In these equations;

ρ: Density

μ: Viscosity (Dynamic)

u: Speed,

P: Pressure

T: Temperature

t: Time

x_i x-y-z: Position tensors

c_p: The Specific Heat

k: Conduction heat transfer coefficient.

The density would not change over time in incompressible flows, thus the conservation equations are arranged as following;

$$\frac{\partial u_i}{\partial x_i} = 0 \tag{4.4}$$

$$\rho \frac{\partial u_i}{\partial t} + \rho \frac{\partial u_i u_j}{\partial x_j} = -\frac{\partial P}{\partial x_i} + \frac{\partial}{\partial x_j}\left[\mu\left(\frac{\partial u_i}{\partial x_j} + \frac{\partial u_j}{\partial x_i}\right)\right] \tag{4.5}$$

$$\rho \frac{\partial T}{\partial t} + \rho \frac{\partial T u_j}{\partial x_j} = \frac{\partial}{c_p \, \partial x_j}\left(k \frac{\partial T}{\partial x_j}\right) \tag{4.6}$$

4.1.2 k-ε Turbulance Model

Similar to real life and many other engineering problems, almost all flows are turbulent. Although there are not precise definitions sources, turbulence can be briefly described as the irregularity in the motion of a liquid or gas.

A complex, irregular turbulance mechanism that does not obey a particular law is characterized by the Reynolds number (for example, the situation where Re≥2300 for flow in the pipe). Solving the governing equations for a turbulent situation is difficult and time consuming process unless various approaches and simplifications are made. It is possible to facilitate the solution process and shorten the solution time by making changes using various approaches. However, 3D Navier-Stokes

equations can be solved directly with some numerical solution methods (such as DNS). This direct solution method is used in cases where the error function is desired to be minimum.

One of these simplification approaches is Reynolds Decomposition. This approach consists of averaging the fluctuating and instantaneous variables in the governing equations. In this case, velocity and pressure;

$$u_i = U_i + u_i' \tag{4.7}$$

$$p = P + p' \tag{4.8}$$

Here, U and P are average values, while i u′ and p′ refer to the fluctuating part. If we substitute these equations into the governing equations, we obtain the Reynolds Averaged Navier-Stokes (RANS) equations;

$$\frac{\partial U_i}{\partial x_i} = 0 \tag{4.9}$$

$$\rho \frac{\partial U_i}{\partial t} + \rho U_j \frac{\partial U_i}{\partial x_j} = -\frac{\partial}{\partial x_i} P + \frac{\partial}{\partial x_j}\left[\mu \frac{\partial U_i}{\partial x_j} - \overline{u_i' u_j'}\right] \tag{4.10}$$

The term $\overline{u_i' u_j'}$ is called the Reynolds strain tensor and refers to the strain created by fluctuating velocities in turbulent flow. To solve this, Boussinesq's theorem can be used.

The k-ε turbulence model, which is used in many fluid dynamics model solutions, was also used as a solver in this thesis study. The k-ε model numerical solution provides reliable results in various flow and heat transfer problems and is ideal in terms of solution time. For steady and incompressible flows, k and ε have the following definitions;

$$\frac{\partial}{\partial t}(\rho k) + \frac{\partial}{\partial x_j}(\rho k u_j) = \frac{\partial}{\partial x_j}\left[\left(\mu + \frac{\mu_t}{\sigma_k}\right)\frac{\partial k}{\partial x_j}\right] + G_k + G_b - \rho\varepsilon - Y_M + S_k \tag{4.11}$$

$$\frac{\partial}{\partial t}\rho\varepsilon + \frac{\partial}{\partial x_j}(\rho\varepsilon u_j) = \frac{\partial}{\partial x_j}\left[\left(\mu + \frac{\mu_t}{\sigma_\varepsilon}\right)\frac{\partial \varepsilon}{\partial x_j}\right]$$
$$+\rho C_1 S\varepsilon + \rho C_2 \frac{\varepsilon^2}{k + \sqrt{v\varepsilon}} + C_{1\varepsilon}\frac{\varepsilon}{k}C_{3\varepsilon}G_b + S_\varepsilon \tag{4.12}$$

$$C_1 = max\left[0{,}43\frac{\eta}{\eta + 5}\right] \tag{4.13}$$

$$\eta = S\frac{k}{\varepsilon} \tag{4.14}$$

$$S = \sqrt{2S_{ij}S_{ij}} \tag{4.15}$$

In the above equations, G_k refers to the turbulence kinetic energy production depending on the velocity gradient, G_b refers to the turbulence kinetic energy produced by bouyancy, and Y_m refers to the magnitude of expansion dissipation in incompressible flows. C_1 and $C_{1\varepsilon}$ are constant numbers, the Prandlt numbers for k and ε are σ_k and σ_ε, respectively.

4.1.3 Bouyancy Flows

Buoyancy flows refer to fluid motion driven by buoyancy forces, typically arising from density differences within the fluid. When a fluid is subjected to variations in temperature, it can lead to variations in density. This density difference can cause the fluid to flow due to buoyancy forces, which arise from the tendency of denser fluid to sink and less dense fluid to rise. Buoyant flows are commonly observed in natural phenomena such as atmospheric convection, ocean currents, and volcanic eruptions, as well as in engineering applications like heating and ventilation systems, and in industrial processes involving fluids of different temperatures or compositions. This behavior can be briefly expressed as follows;

$$u\frac{\partial u}{\partial x} + v\frac{\partial u}{\partial x} = -\frac{g}{\rho}(\rho_\infty - \rho) + \frac{\mu}{\rho}\frac{\partial^2 u}{\partial y^2} \tag{4.16}$$

This equation is written for two-dimensional incompressible flow. The first element on the right side is the buoyancy forces caused due to density change. Boussinesq

states that the density change in buoyancy currents is small, so they do not take the density change into consideration. We have already stated that the density change is caused by the change in temperature, so we need to add the temperature term to our equation. The thermal expansion coefficient β expresses the density change that occurs as a result of the temperature change at constant pressure in buoyancy flows. In this situation;

$$\beta = -\frac{1}{\rho}\frac{\partial p}{\partial T}\Big|_p \approx -\frac{1}{\rho}\frac{\rho_\infty - \rho}{T_\infty - T} \tag{4.17}$$

$$\rho_\infty - \rho \approx \rho\beta(T - T_\infty) \tag{4.18}$$

The momentum equation in gravitational direction is formed as;

$$u\frac{\partial u}{\partial x} + v\frac{\partial u}{\partial x} = -g\beta(T - T_\infty) + \frac{\mu}{\rho}\frac{\partial^2 u}{\rho\,\partial y^2} \tag{4.19}$$

For ideal gases β is the reciprocal of the total temperature. It can be expressed as follows;

$$\rho = \frac{p}{RT} \tag{4.20}$$

$$\beta = -\frac{1}{\rho}\frac{\partial p}{\partial T}\Big|_p = \frac{1}{\rho}\frac{p}{RT^2} = \frac{1}{T} \tag{4.21}$$

4.1.4 Heat Transfer Mechanisms

The transfer of energy through conduction, convection and radiation between two or more objects that have different temperatures is defined as heat transfer. These heat transfer forms will be briefly mentioned.

4.1.4.1 Heat Transfer By Conduction

Conduction heat transfer is the heat transfer mechanism formed by energy transfer and random molecular movements due to the temperature difference in an environment. The moment equation for this mechanism is known as Fourier's Law

and for a flat wall with temperature distribution T(x) in one direction is expressed as following;

$$q_x^{ll} = -k\frac{dT}{dx} \tag{4.22}$$

q is the heat flux passing through the wall per unit surface in unit time, dT/dx is the heat gradient in this direction. To get from this heat flux formula to the heat value, we need to multiply the area (A) by the right side of the equation.

The same formula is valid for structures we call mixed walls consisting of several levels. However, the combined heat transfer coefficient must be calculated. Because of this, complex walls are solved by finding the equivalent thermal resistance (R) by taking advantage of the similarity between electric current and heat current. Following equations can be used for a wall with n layers parallel to each other;

$$q_x = \frac{T_{\infty,1} - T_{\infty,n}}{\sum R} \tag{4.23}$$

$$\sum R = \frac{1}{h_1 A} + \frac{L_1}{k_1 A} + \frac{L_2}{k_2 A} + \cdots + \frac{L_n}{k_n A} + \frac{1}{h_2 A} \tag{4.24}$$

$$k = \frac{1}{R} \tag{4.25}$$

4.1.4.2 Heat Transfer By Convection

Convection heat transfer is the heat transfer mechanism between a surface and a fluid. Heat transfer takes place between the currents in the fluid and the surface. It is formulated as follows;

$$q^{ll} = h(T_s - T_\infty) \tag{4.26}$$

In this formula, h is the convection heat transfer coefficient, T_s is the surface temperature, T_∞ is fluid temperature. The convection heat transfer coefficient is calculated using the flow theory for 2 dimensional surfaces and is a function of the Prandlt (Pr) number;

$$Nu_x = \frac{hx}{k} \tag{4.27}$$

$$Nu_x = 0.0288\mathrm{Pr}^{\frac{1}{3}}\ \mathrm{Re}^{0,8} \tag{4.28}$$

$$\mathrm{Re}^2 = \frac{Ux}{v} \tag{4.29}$$

Pr is the Prandlt's number, Nu_x is the Nusselt's number, Re is the Reynolds' number, k is the conduction heat transfer coefficient of the surface, x is the length of the surface, ν is the viscosity of the fluid, and U is the flow rate on the surface.

4.1.4.3 Heat Transfer By Radiation

The energy released by an object having a limited temperature is known as thermal radiation. Electromagnetic waves transport the radiation field's energy. Radiation does not require the presence of a material medium, in contrast to energy transfer via conduction or convection. Contrary, radiative transfer take place more effectively in the vacuum. The radiation emitted by a surface originates from the thermal energy of the. The energy released from the surface per unit time is called the emissivity of the surface E. The Stefan-Boltzman law defines an upper limit to the emissivity;

$$E_b = \sigma T_s^4 \tag{4.30}$$

In this equation, T_s is the absolute temperature of the surface, σ is the Stefan-Boltzman constant ($\sigma=5.67\text{x}10^{-8}$ W/m^2.K^4). This kind of surfaces are referred to as a black surfaces or ideal radiators. The following equation represents the heat flux that a real surface emits at a particular temperature; it is less than the heat flux that a black body emits at the same temperature;

$$E_b = \varepsilon\sigma T_s^4 \tag{4.31}$$

In the above equation, ε is radiative property of the surface and is called emissivity. It can take values between 0 and 1, it is the ratio of the energy emmited comparing to a black body. It is the thermal radiation coming from the surroundings on a surface. Sun and other surfaces within the perfpective of the surface are examples to to radiation sources. All of the radiation induced on the unit surface area over time is called induced radiation (G).

Some or all of the incoming radiation can be absorbed by the surfaces, and therefore the thermal energy of the material increases. The radiant energy absorbed per unit area of the surface per unit time can be calculated if the absorption rate α, which is a radiative property of the surface, is known. According to this It is defined by the following equation;

$$G_{abs} = \alpha G \tag{4.32}$$

If the surface is radiation-proof α<1, some of the radiation is reflected. If the surface is semi-permeable, some of the incoming rays pass through, some are absorbed, and the rest are reflected. In this situation the following equation is obtained;

$$\alpha + \rho + \tau = 1 \tag{4.33}$$

α is the absorption, ρ is the reflected and τ is the transmitted radiation ratios. Kirchoff's law examined in which cases the emission rate and absorption rate are equal. Based on this, the gray body definition was made. Accordingly, the gray body can be simply defined as the surface where the emission and absorption rates are equal, regardless of wavelength. In this case, we will see that for an opaque surface;

$$\alpha + \rho = 1 \tag{4.34}$$

$$\rho = 1 - \varepsilon \tag{4.35}$$

And if we write the enery equation we would get;

$$q_{out,k} = \varepsilon_k \sigma T_k^4 + \rho_k q_{in,k} \tag{4.36}$$

4.1.5 Wall Functions

Wall equations are used to approximate variables such as turbulence, velocity and pressure near the wall (in the boundary layer) where the flow occurs. In solutions without using this approach, if the boundary layer is desired to be examined, it must be very thinly meshed near the wall, which means a long solution time. For this reason, wall functions are used to examine the boundary layer in many problems. The wall equations express the velocity profile in the logarithmic domain as following;

$$u^+ = \frac{\overline{v_t}}{u_\tau} = \frac{1}{\kappa}\ln(y^+) + B \tag{4.37}$$

In the equation, $\overline{v_t}$ is the is the average velocity parallel to the wall, uτ is the shear velocity, κ is the Karman constant (~0.41), B is the viscous layer thickness found empirically, and y^+ is the dimensionless distance from the wall. These terms are defined as following;

$$u_\tau = \sqrt{|\tau_w|\rho} \tag{4.38}$$

τ_w is the shear strain in the wall,

$$y^+ = \frac{\rho u_\tau y}{\mu} \tag{4.39}$$

5
MODEL DEVELOPMENT

5.1 Study Case

A plug in hybrid vehicle Li-Ion High Voltage battery pack consistsing of 4 (160s2p) short and 3 long stacks of (160s3p) is cooled with 4 short and 3 long cooling plates. A simplified cooling cirvuit can be seen in Figure 5.1. Due to package constraints the cooling plates are having off-centrig inlet and outlet spigots that cause the coolant flow to be unevenly distributed within the cooling plate channels. The geometry where the inlet coolant flow is non centric to the cooling plate and needs to expand in very short length can be seen in the section cut view of the inlet manifold cooling plate assembly in figure 5.2. Non uniform mass flow caused due to this geoemtry through the cooling plate channels requires to be optimized in order to prevent early aging due to uneven cooling of battery cells.

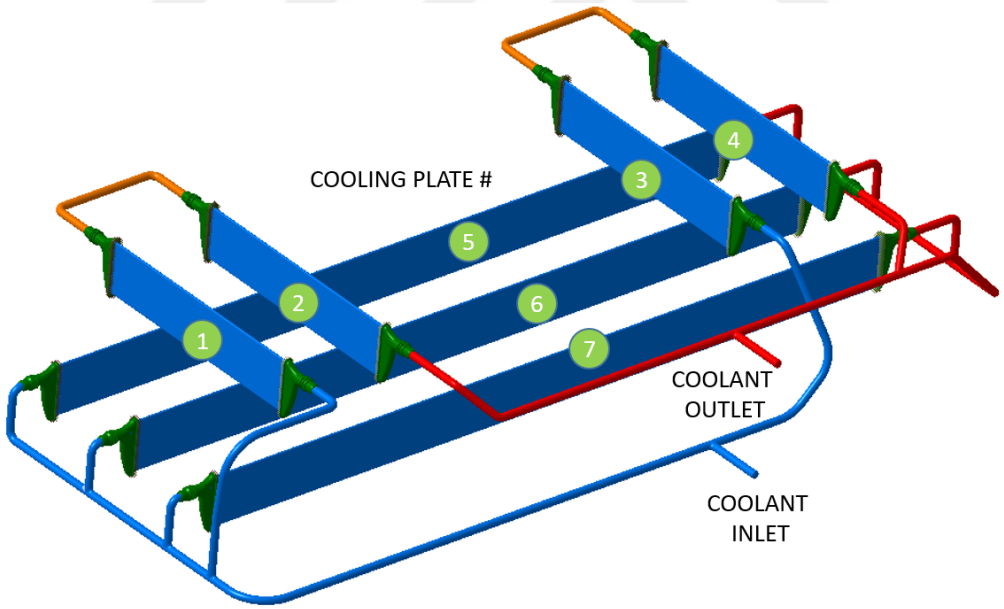


Figure 5.1 Battery pack cooling system layout

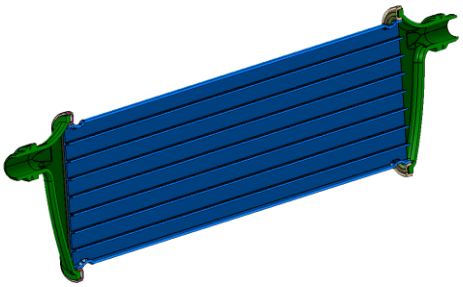


Figure 5.2 Isometric section view of the cooling plate showing internal channels

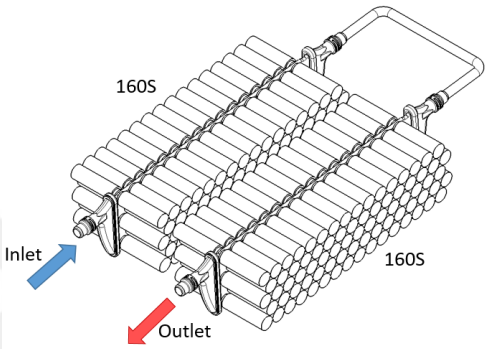


Figure 5.3 Single battery stack module

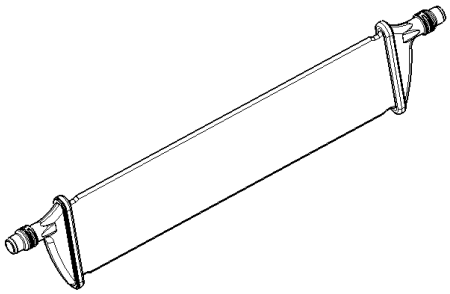


Figure 5.4 Coolant plate

As it can be seen in the Figures 5.1 and 5.3 the cooling circuit is serially connected to 2 short cell stacks of 160s2p cell configuration. This means the outlet tmperature of the first stack is close to be inlet temperature of the second stack. Figure 5.4 shows the cooling plate prior to be assembled in the cell stack.

The coolant mass flow and inlet outlet tempertures are calculated on a separate vehicle level model. Vehicle load cases showed that the thermal sizing case to be the fast carging use case due to its high continuous current and long duration, also

the vehicle not being in motion having only fan air running through the condenser. The boundary conditions have been set as the following;

Table 5.1 Boundaty conditions

Coolant mass flow for short plate:	2.3 L/min
Coolant mass flow for long plate:	3.55 L/min
Coolant temperature:	25˚C
Ambient temperature:	35˚C
Max battery cell temperature:	40˚C
Load case:	Charge @1C
Flow targets:	Coolant flow form to stay laminar
Coolant flow speed	To not exceed 0.7m/s at any point

STAR CCM + CFD analysis tool is used for the thermal loads and flow analysis.

5.2 Long Cooling Plate Flow Analysis Results

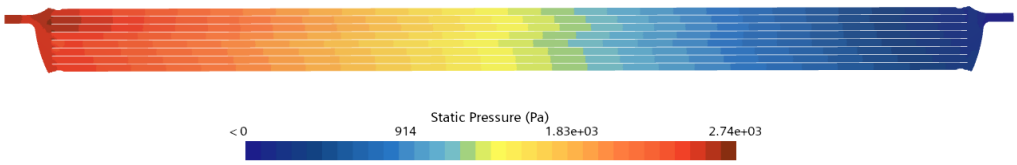


Figure 5.5 Long cooling plate pressure drop analysis result



Figure 5.6 Long cooling plate fluid velocity analysis result

Figures 5.5 and 5.6 is shows the CFD results for the pressure drop and coolant velocity through out the long cooling plate.

Long cooling plate pressure drop is read as 2590Pa

Long Cooling plate max fluid velocity is read as 0.72m/s

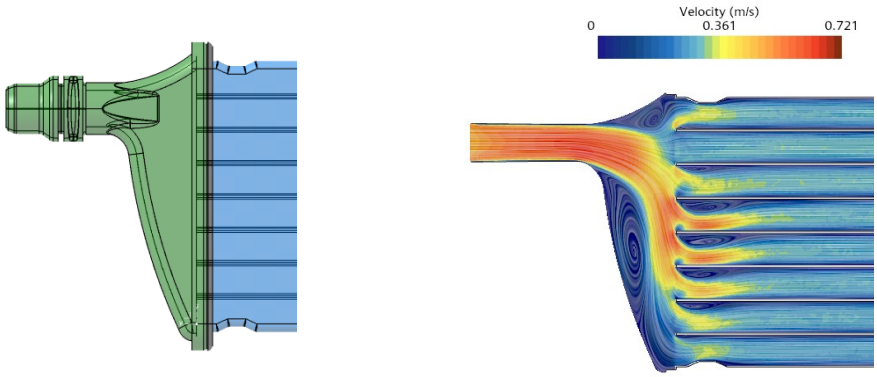


Figure 5.7 Long cooling plate end tank and coolant flow distribution from inlet spigot to channels

Figure 5.7 shows how the coolant flow from the inlet spigot throught the manifold and then distributed into the long cooling plate channels.

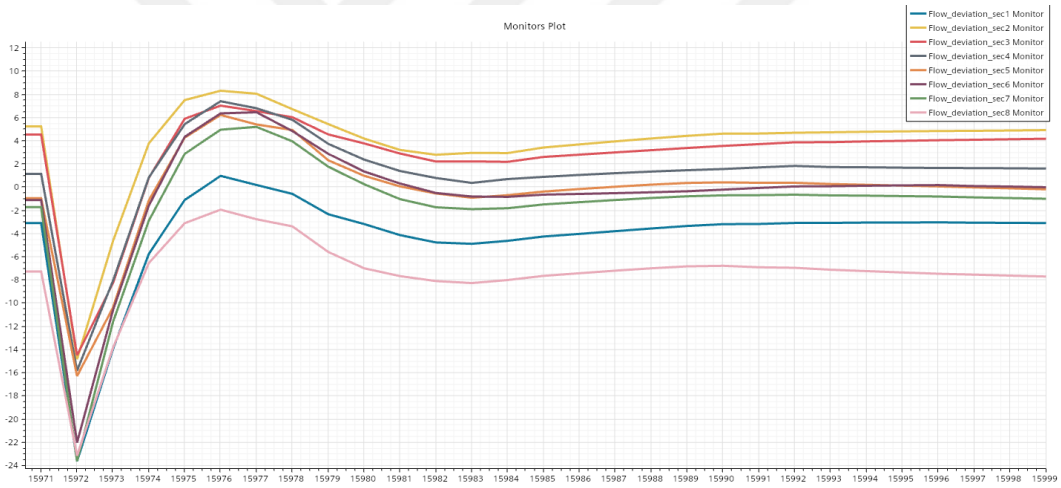


Figure 5.8 Long cooling plate channels fluid mass flow deviation from average CFD Analysis Result

Figure 5.8 shows, the deviation on the massflow from the perfect distrubtion on each channel of the long cooling plate. The values are given in the Table 5.2

Table 5.2 Long cooling plate channels fluid mass flow deviation from average CFD Analysis Result

Channel Number:	Deviation from target (%)
CH1	+6.27
CH2	-2.72
CH3	5.24
CH4	1.39
CH5	-1.14
CH6	-1.41
CH7	-1.89
CH8	-7.90

5.3 Short Cooling Plate Flow Analysis Results

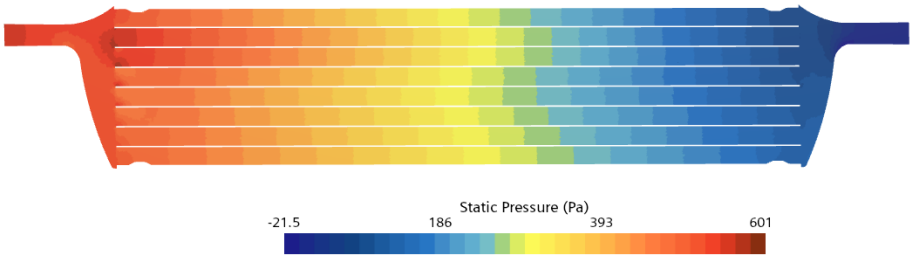


Figure 5.9 Short cooling plate pressure drop analysis result

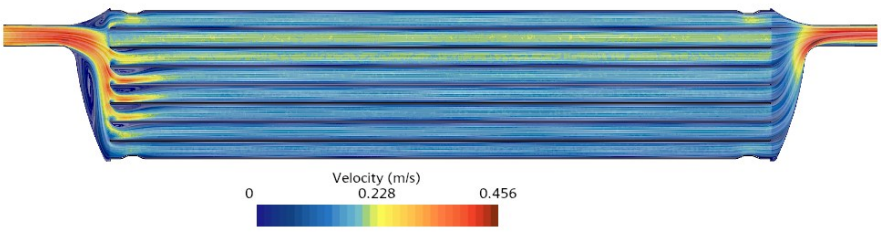


Figure 5.10 Short cooling plate fluid velocity analysis result

Figures 5.9 and 5.10 is shows the CFD results for the pressure drop and coolant velocity through out the long short cooling plate.

Short cooling plate pressure drop is read as 550Pa

Short cooling plate max fluid velocity is read as 0.46m/s

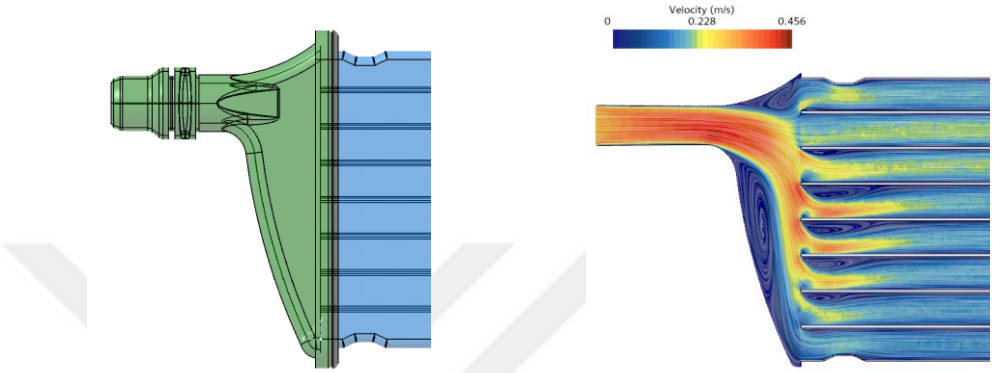


Figure 5.11 Short cooling plate end tank and coolant flow distribution from inlet spigot to channels

Figure 5. 11 shows how the coolant flow from the inlet spigot throught the manifold and then distributed into the short cooling plate channels.

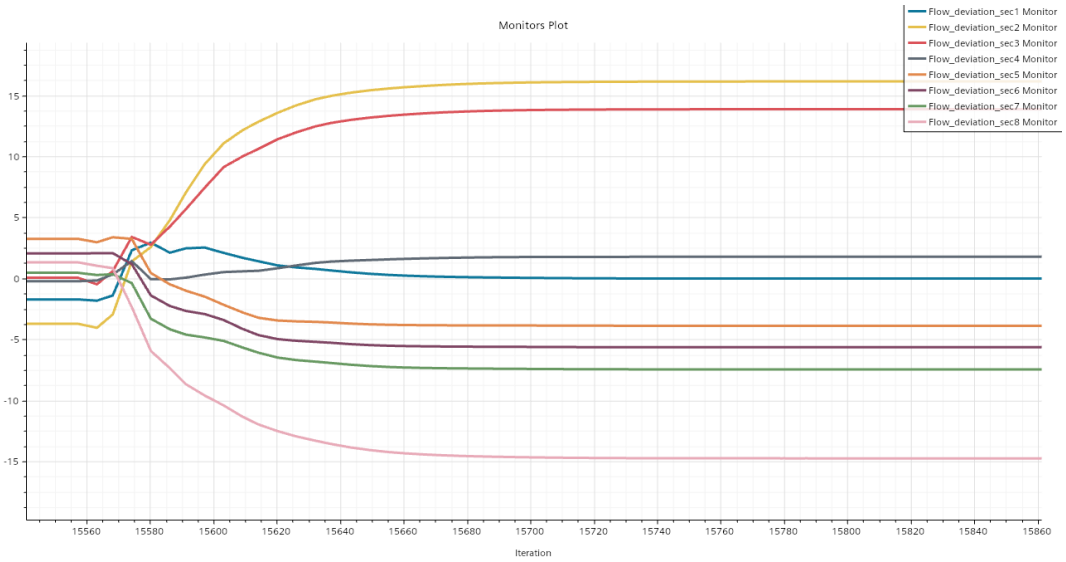


Figure 5.12 Short cooling plate channels fluid mass flow deviation from average CFD Analysis Result

Figure 5.12 shows, the deviation on the massflow from the perfect distrubtion on each channel of the short cooling plate. The values are given in the Table 5.3

Table 5.3 Short cooling plate channels fluid mass flow deviation from average CFD Analysis Result

Channel Number:	Deviation from target (%)
CH1	-0.02
CH2	+16.14
CH3	+13.87
CH4	+1.77
CH5	-3.88
CH6	-5.64
CH7	-7.45
CH8	-14.74

Initial Flow analysis results how that whilst we have only 2 outliner channels with more than +/- 5% mass flow deviation in the long cooling plate, we have 5 in the short cooling plate. Also the deviation values of the short cooling plate are missed by much bigger margins with comparison to the long cooling plate. The main reason of this is short cooling due to its length not creating enough back pressure withiin the cahnnels facing the spigots, and the flow finding itself an easy escape to the outlet. The misses in the long cooling plate are found to be not value add for investment and the short cooling plate has been chosen for optimization. Hence the analisys results from long cooling plate are usedon determining the boundary conditions of the short cooling plate optimization study.The maximum pressure drop target is proportionally calculated and the fluid speed is taken carry over to the shot cooling plate.

5.4 Thermal Load Calculation

One stack consist of 320 x 21700 form Li-ION NMC cells

The cooing plate is Aluminium

Coolant used is 50/50 ethylene glycol mix

Table 5.4 shows the attribute and properties to be used for the thermal load calculation;

Table 5.4 Physical properties

	Coolant	21700 Cell	Aluminium
Density (kg/m^3)	1060	2475	2702
Heat Capacity (J/kg°K)	3300	1040	903
Thermal Conductivity (W/m°K)	0.414	N/A	237
Radial Thermal Conductivity (W/m°K)	N/A	5	N/A
Axial Thermal Conductivity (W/m°K)	N/A	30	N/A

Table 5.5 HV battery cell specification

Cell Brand / Model	SAMSUNG INR21700-50E	
Internal Resistance (DCIR) (mOhm)	45	
Discharge Capacity (mAh)	4900	
Min Voltage (V)	2.5	
Nominal Voltage (V)	3.63	
Maximum Voltage (V)	4.20	
Charging Voltage (V)	4.20	
Max Charging Current (A)	4,9	1C
Max Discharge Current (A) Continuous	9.8	2C
Max Discharge Current (A) Momentarily	14.7	3C
Volume (cm^3)	22.8	
Weight (g)	69.5	
Operating Temperature (Charge) (˚C)	0 to 45	
Operating Temperature (Discharge) (˚C)	-20 to 60	
Density (kg/m^3)	3050	

Table 5.5 shows the techniocal specifications of the lithium ion battery cell

5.5 Boundary Conditions

Among charging and discharging use cases, fast charging case has been found as the most thermally critical case due to its continuous high current flow.

This case is using 4.9A current the fast charging case. Table 5.6 shows the boundary conditions and design targets dictated by design rules and range of system and vehicle attributes.

Table 5.6 Design boundary conditions and targets

Ambient Temperature (˚C)	35	
Max Cell Temperature (˚C)	40	
Max Cell Temperature gap (˚C)	5	
Coolant Inlet Temperature (˚C)	25	
Max Coolant Temperature Increase (˚C)	3	
Maximum pressure drop on Cooling Plate (Pa)	800	
Max fluid speed in cooling plate (m/s)	0.7	
Flow type	Laminar	Reynolds<2300
Battery Load Condition	1C	Charging

5.6 Calculation of the Thermal Loads and Fluid Mass Flow

We need to calculate the steady state heat dissipation from the cell stack. We can do that by multiplying the brochure DCIR number with number of cells and with the square of our target charging current (C) rate.

$$P = (\text{Cell Charging Current})^2 * \text{DCIR} * \text{Cell Count} \quad (5.1)$$

$$P = 4.9*4.9*0.045*320 = 345W$$

Required coolant mass flow based on the target ΔT that will be able to discharge the excess heat out from the cell stack can be calcualted with the following equation;

$$P = 345W$$

$$cp* \dot{V} *\Delta T$$

$$\dot{V} = P / cp \ / \Delta T / \rho \quad (5.2)$$

$$= 345 /1060/3300/3 = 3.3E\text{-}5\ m^3/s = 0.35kg/s$$

5.7 Thermal Conductance Calculation

We also need to measure if the amount of the cooling discharge required can be conducted through the thermal path.

There is a thermal paste between the cells and the cooling plate.

The thermal paste diameter is 16mm for each cell (out of 21mm cell diameter) and the thickness is 4mm

The thermal conductivity of the thermal paste is 8W/m˚K

The conductance rate can be found using following equation;

$$Q=k*(T_2-T_1)/L \quad (5.3)$$

$$Q=8*(35-25)/(4*10^{-3})=20.000\ Watt$$

$$P(\text{Heat discharge power})=Q*A \quad (5.4)$$

$$20.000 * (16/2*10\text{-}3)2*PI *320(cells) = 1286\ Watt > 345Watt$$

The thermal path has higher conductance than required heat discharge, means the heat can be discharged as long as the temperature difference is maintained.

5.8 Finite Element CFD Model Build

Two different models were created for the assessments in the study;

1 – Thermal Assessment Model
2 – Flow Optimization Model

5.8.1 Thermal Assessment CFD Model

This CFD model was created to assess the thermal path and the temperature distribution under the set boundaries. Different physic properties have been assigned to the components. Whilst the thermal path has been meshed finer the non thermal path, such as PP material end tanks are meshed coarse (10mm). Table 5.7 summarizes the element numbers of different componenets of the assembly.

Table 5.7 Mesh cell, face and vert numbers for the CAE model components

Fluid Volume:	761025 cells, 3108950 faces, 2967197 verts.
Thermal Paste Left :	235182 cells, 950516 faces, 823130 verts.
Thermal Paste Right :	239615 cells, 966068 faces, 799845 verts.
Cells Left :	986145 cells, 4467631 faces, 3001619 verts.
Cells Right:	979048 cells, 4434266 faces, 2989263 verts
End tank Inlet:	58869 cells, 264048 faces, 213003 verts.
End Tank Olet:	58864 cells, 264281 faces, 206393 verts
Sealant Inlet:	13550 cells, 53706 faces, 46271 verts.
Sealant Outlet:	13568 cells, 53844 faces, 46342 verts.
Aluminum Plate:	2342889 cells, 10218395 faces, 7739558 verts.

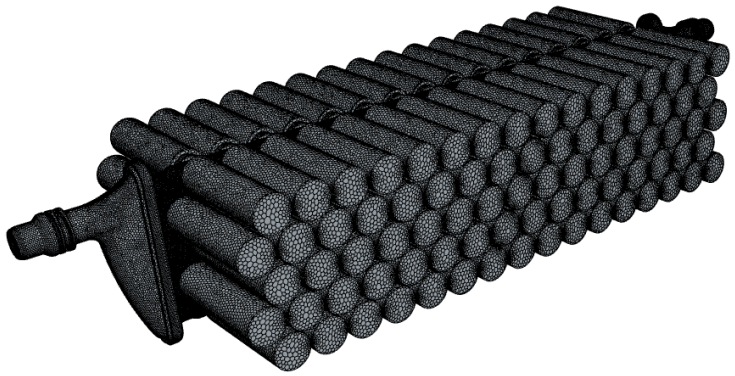


Figure 5.13 Battery cell stack mesh view

The mesh form and denisty can be viewed on Figure 5.13

Enabled FE models for solid materials are gradients, segregated solid energy, constant denstiy, solid, steady, solution interpolation and three dimensional.

Enabled FE models for fluid materials are coupled energy, polynomal density, laminar flow, gradients, coupled flow, liquid, steady, solution interpolation and three dimensional.

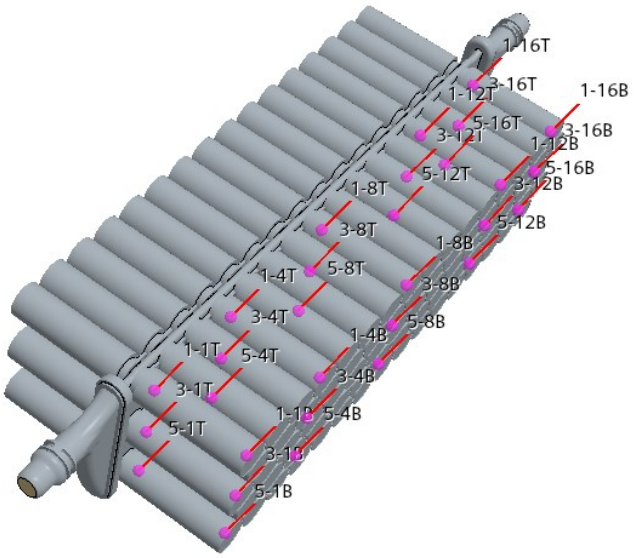


Figure 5.14 Thermal model measurement points

Figure 5.14 shows the temperature measurment points in the single cell stack. Measuremnt is taken from 15 cells out of 30, 1 temperature point is selected on the thermal paste face and one on the furthest point from the cooling plate.

5.8.2 Flow Optimisation CFD Model

This CFD model is built to assess and optimize the deflector design and reduce the mass flow variation between the channels

Original (Model): 3254302 cells, 13384597 faces, 7572911 verts.



Figure 5.15 Cooling plate coolant fluid volume mesh model

The mesh mode of the coolant fluid can be seen in Figure 5.15. Both models have been set to use the following Mesh parameters,

Table 5.8 Mesh parameters

Mesh Type:	Polyhedral Triangle
Base size:	4mm – 10mm
Number of prism layers:	10
Prism Layer stretching:	1.2
Target surface size :	100%
Min surface size :	10%

5.8.3 Prism Layer Settings

We initially have run the analysis with 6 prism layers at the wall boundaries. In order to understand if we selected adequate number of prism layers, we have run the same analysis with 10 prism layers and compared the results. One set has been run with no deflector and another set has been run with deflector iteration no:9.

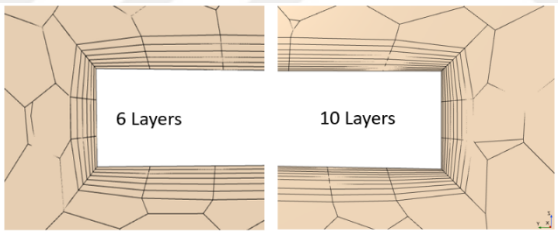


Figure 5.16 Prism layer comparison on wallfluid boundary

Table 5.9 Prism layer 6 & 10 comparison CFD flow results for base (No deflector) design

Without deflector	Deviation (%) 6 Prism Lavers	Deviation (%) 10 Prism Lavers	Change (%) Change (massflow) (kg/s)
Mesh Count	1897871	2910761	53.37%
Channel 1	-0.02	-0.01	-0.50%
Channel 2	16.14	16.23	0.01%
Channel 3	13.86	13.87	0.00%
Channel 4	1.77	1.75	-0.01%
Channel 5	-3.88	-3.90	0.01%
Channel 6	-5.64	-5.67	0.01%
Channel 7	-7.45	-7.47	0.00%
Channel 8	-14.75	-14.75	0.00%

Table 5.10 Prism layer 6 & 10 comparison CFD flow results with (No 9 deflector) design

With Deflector Option 9	Deviation (%) 6 Prism	Deviation (%) 10 Prism	Change (%) cells Change (massflow)
Mesh Count	2118328	3254302	53.63%
Channel 1	0.79	0.73	-0.08%
Channel 2	0.70	0.60	-0.14%
Channel 3	-0.5	0.54	-2.08%
Channel 4	0.14	0.128	-0.09%
Channel 5	1.02	1.00	-0.02%
Channel 6	-0.06	-0.028	-0.53%
Channel 7	-0.1	-0.085	-0.15%
Channel 8	-1.39	-1.21	-0.13%

On tables 5.9 and 5.10 it can be observed that the number of prism layers are increasing the mesh numbers above 50% per model whilst the greater change on

the results is found to be 2% on a single channel. This can be considered within the tolerance of the CFD tool.

5.9 Pre Optimisation Thermal Status

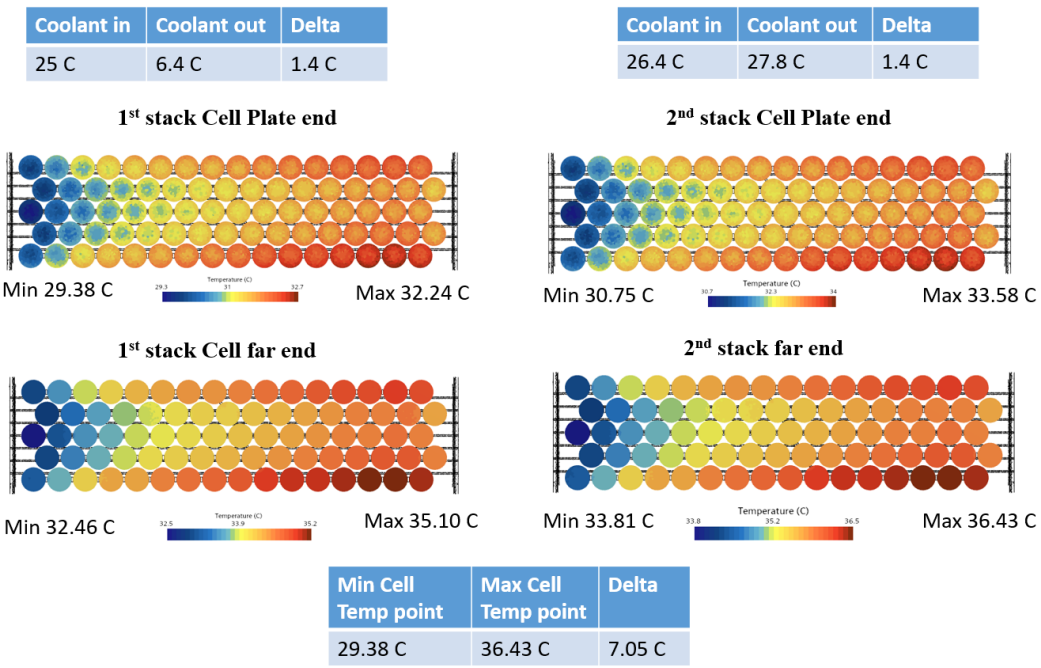


Figure 5.17 Thermal analysis legend before flow optimisation and min max temperatures taken from extreme points of the cells

In figure 5.17 can be seen that the bottom end cells that are away from coolant inlet and outlet spigots are struggling with keeping up with the max maximum 5˚C degree gap target. This is thought to be the particular coolant channels lacking mass flow whilst the middle top channels are getting much higher mass flow. This will be evaluated and then optimised with speed flow analysis.

5.10 Pre Optimization Thermal Status

We are going to use flow deflector to optimize the mass flow deviations on the cooling plate channels.

A deflector is designed to guide the coolant mass flow evenly through the each cooling plate channel. Distance to spigot center point is used as a guide to determine hydraulic diameters for the deflector separation. The optimum coolant flow distribution has been reached with 9 design iterations. Reynolds number is

calculated for each channel and targeted to be below 2300 to make sure the flow stays laminar.

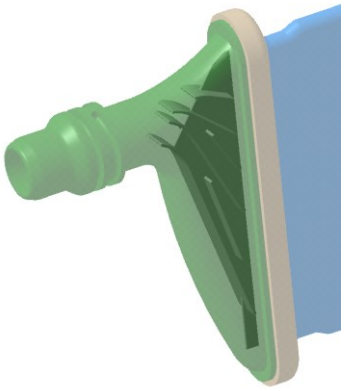


Figure 5.18 Inlet manifold spigot with deflector inside

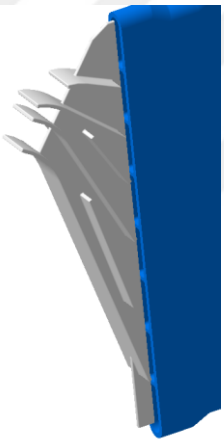


Figure 5.19 Deflector in front of cooling plate

As a starting point the hydraulic diameter of the each deflector entrance is being proportionally calculated based on each channels entry point distance to the spigot exit. Figures 5.18 and 5.19 shows the initial flow deflector design generated to guide the flow evely into the cooling plate channels.

Figure 5.20 shows the straight line distances of each cooling plate channel form the inlet spigot. Figure 5.21 shows the stream channels created by the deflector geometry.

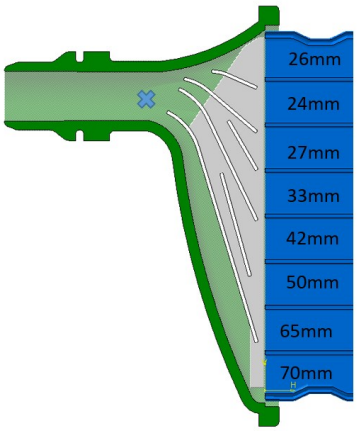


Figure 5.20 Channel entry point distances to spigot reference point (straight distance)

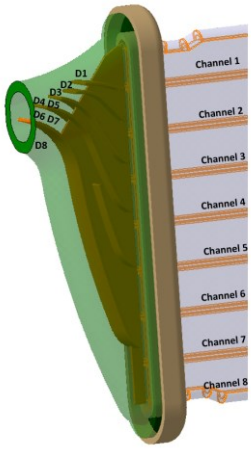


Figure 5.21 Deflector entrance and deflector exit geometries

The inlet spigot of the end tank is transitioning from a 12mm diameter circle into 12mm wide rectangular. The deflector surfaces are positioned in such way to deflect equal amount of coolant mass flow into the aluminium cooling plate's channels. In order to have equel mass flow in the channels we need to ensure there is equal amount of pressure loss on each channel.

Friction and momentum exchanges caused by the changes the directon of the flow causes the pressure losses in the pipes. Bend angle, the ratio of the radius and channel diameter, as well as the Reynolds number are effecting the pressure drop amount. The total pressure of the particular channel in the coolng plate we are investigating can be broken down into 3 elements. The overall friction losses on the

overall length of the particular channel, the inlet flow direction changes and outlet direction changes.

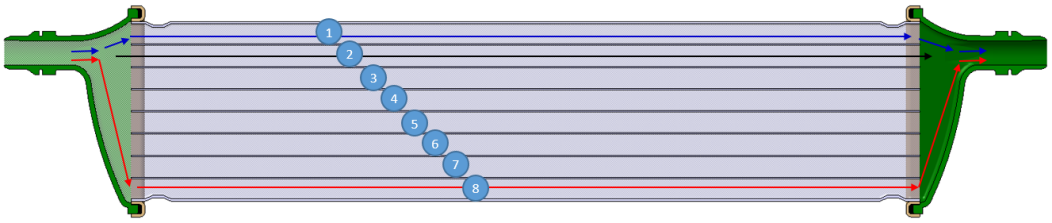


Figure 5.22 Cooling plate internal channels and fluid flow routes

Figure 5.22 represents the different angles the flow needs to follow in order to be distributed inside the cooling plate channels. The flow is entering the inlet end tank and needs to change direction with an angle to target the channel entrance, then it needs to change direction with secondary angle to enter the channel, and followd the symetric route to enter and leave the outlet end tank.

As it can be seen in figure 5.22 the channels 2, 1 and 3 are having advantage of having less pressure drop due to momentum losses and shorter length reducing the friction losses. The pressure drop on a bend geometry can be calculated with the following equation.

$$\Delta P = \frac{1}{2} f_s \rho v^2 \frac{\pi R_b}{D} \frac{\theta}{180} + \frac{1}{2} k_b \rho v^2 \qquad (5.5)$$

ΔP : Pressure Drop

f_s : Moody friction factor

ρ : Density

v : Mean flow velocity

R_b : Bend radius

D : Tube Hydraulic diameter

Θ: Bend angle

k_b : Bend loss coefficient

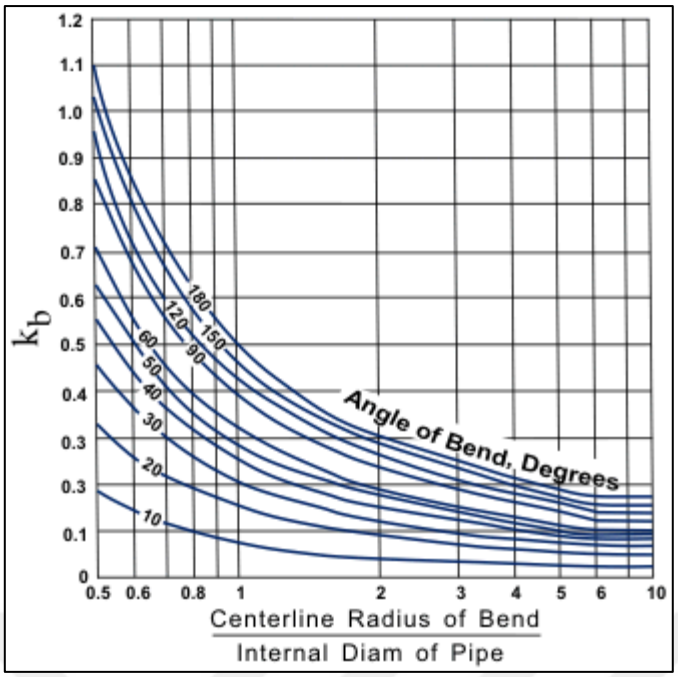


Figure 5.23 Bend loss coefficients for a pipe

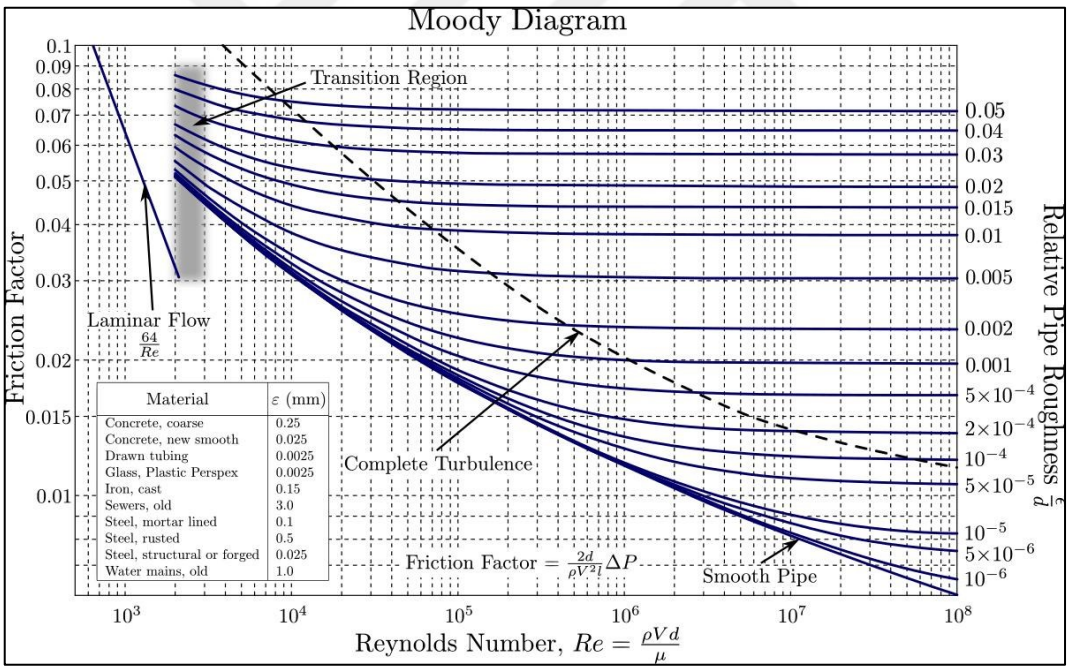


Figure 5.24 Moody friction diagram

Figure 5.23 shows the bend loss coefficient diagram, and figure 5.24 is shown Moody's friction diagram showing the relation between Reynolds number, friction factor and relative pipe roughness.

On top of the bend losses there will be friction loss along each channel. And these can be calculated using Darcy–Weisbach Equation. The equation calculate the pressure drop in a pipe is;

$$\Delta P = fL\rho V^2/2Dh \quad (5.6)$$

ΔP: Delta Pressure (Pa)

f: Darcy friction factor (dimensionless)

L: Pipe length (m)

Dh: Pipe hydraulic diameter (m)

ρ: Fluid density (kg/m^3)

V: Flow velocity (m/s)

Since the internal width of the end tanks is constant, and the mass flow we would like to achieve in each channel is known we can roughly calculate the initial height of each inlet stream channel using these two equations.

5.11 Reynolds Number Investigation

We need to check that the flow is staying laminar in the deflector stream sections in order to ensure we are using the correct analysis model. Therefore the Reynolds numbers for critical sections are calculated using the extreme values.

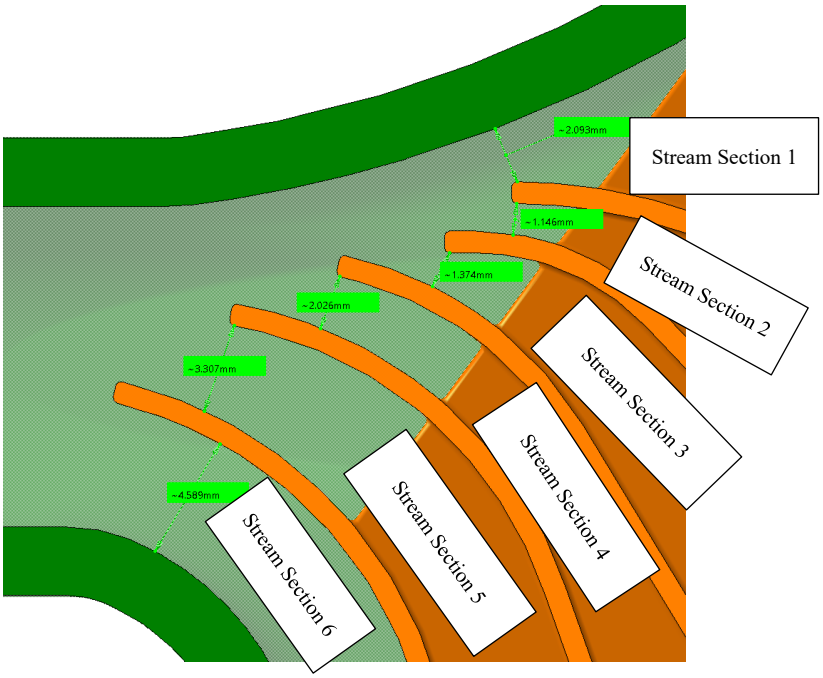


Figure 5.25 Coolant flow stream channels

Figure 5.24 shows how the new coolant flow stream channels are generated with the deflector design and their hieght.

Reynolds number is calculated with the following equations using the dynamic viscousity of the fluid;

$$Re = \frac{\rho v d}{\mu} \tag{5.7}$$

In this equation; *Re:* Reynolds number, ρ:density of the fluid, v :the velocity of the flow, d : hydraulic diameter of the stream section, μ : dynamic viscousty of the fluid.

The properties of the 50-50 water ethylene-glucol coolant we are using are as follows;

ρ (Density) = 1.06E+3 kg/m^3

μ (Dynamic viscousity) = 3.84E-03 Ns/m^2

V_h (high speed Flow speed) = 0.7 m/s

V_l (high speed Flow speed) = 0.15m/s

Table 5.11 Reynolds numbers calculated for each stream section channel

	Height	Width	Dh	μ dynamic Vicousity	Flow Speed	Reynolds Number	Flow Type
	m	m	m	Ns/m^2	m/s	High Speed Flow	
Section 1	2.10E-03	3.70E-03	2.68E-03	3.84E-03	0.7	111.6	Laminar
Section 2	1.14E-03	3.70E-03	1.74E-03	3.84E-03	0.7	72.6	Laminar
Section 3	1.40E-03	3.70E-03	2.03E-03	3.84E-03	0.7	84.61	Laminar
Section 4	2.00E-03	3.70E-03	2.60E-03	3.84E-03	0.7	108.15	Laminar
Section 5	3.30E-03	3.70E-03	3.49E-03	3.84E-03	0.7	145.31	Laminar
Section 6	4.60E-03	3.70E-03	4.10E-03	3.84E-03	0.7	170.83	Laminar

As the speed is proportional with the Reynolds number we use our boundary condition for max fluid speed 0.7m/s as the highest speed.

The hydraulic diameter on top and bottom stream sections is half circle. So it is hard to calculate, but we would re-evaluate these numbers in case they come at critical region.

When we put all the values into the equation we find the following Reynolds numbers for the critical stream sections. It is observed that renolds numbers are at around 10% of the 2300 Reynolds number where the transient flow begins. Calculation results in Table 5.11 show all stream channels are staying in laminer flow. There have been 9 major design iteration to reduce the mass flow deviations within the 9 channels of the cooling plate.

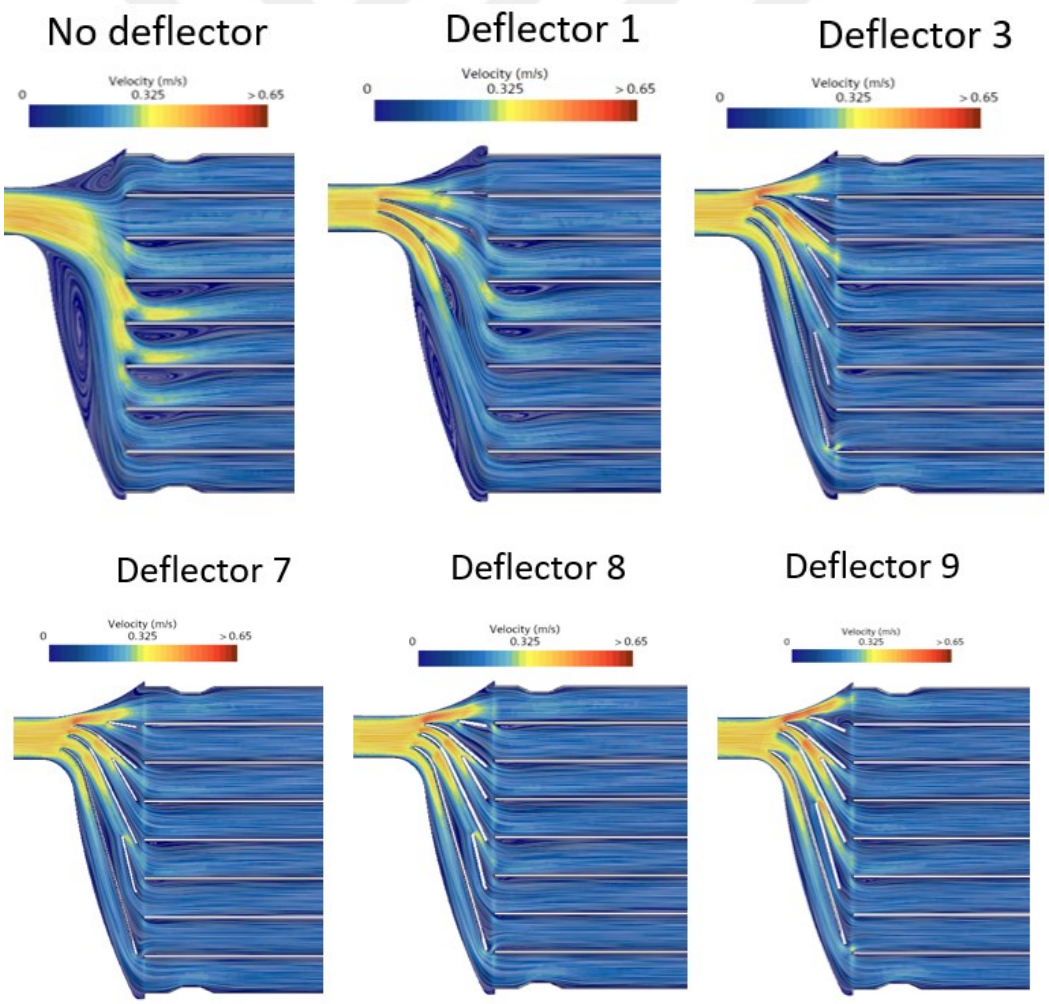


Figure 5.26 Notable deflector design iterations

On Figure 5.26 can be observed how the flow is smoothened to parallel and offset layers, the vortex formations are also reduced thoughout the design iterations.

5.12 Initial Optimisation Results

Figure 5.27 shows the pressure drop following the initial optimization that stays below the max pressure drop targeted. The improvement on the flow streams and the reduced vortex forms following the initial optimisatin study can be observed in figure 5.28.

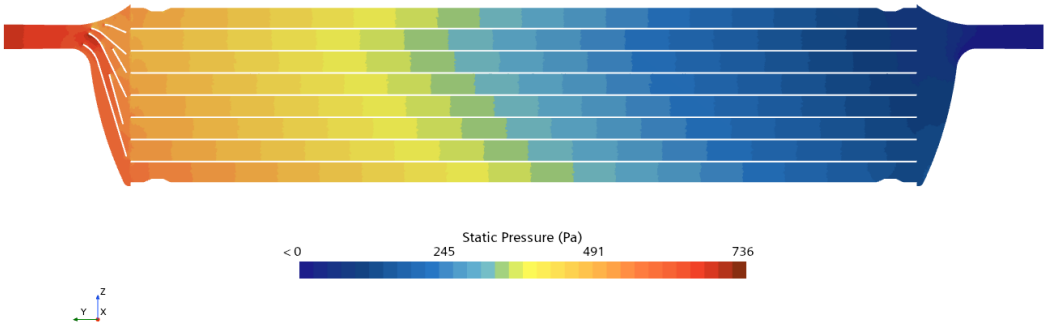


Figure 5.27 Post optimisation cooling plate pressure drop status

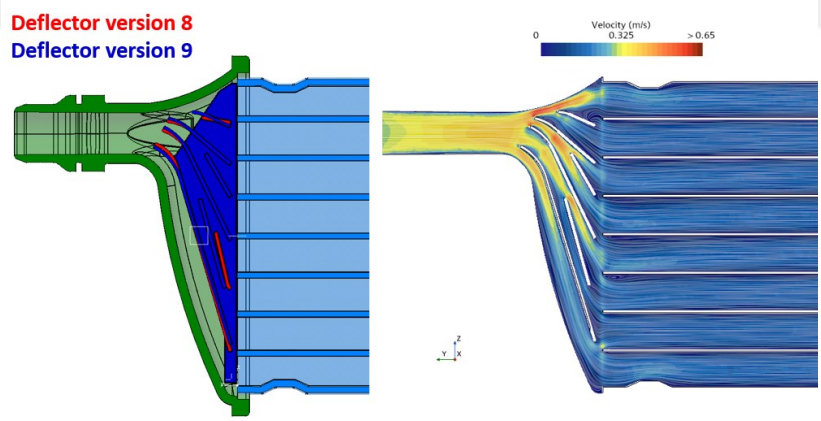


Figure 5.28 Post optimisation channel mass flow deviations

Table 5.12 shows the comparison of the mossflow deviation values before and after initial optimisation study. Post optimisation the deviation on coolant massflow on channels has been reduced from 14-16% levels to ~1% levels.

Table 5.12 Pre and post initial optimisation flow deviation comparison

	Pre Optimisation	Post Optimisation
	Deviation from target (%)	Deviation from target (%)
CH1	-0.02	+0.48
CH2	+16.14	+0.65
CH3	+13.87	+0.44
CH4	+1.77	+1.27
CH5	-3.88	-0.64
CH6	-5.64	-0.52
CH7	-7.45	-0.43
CH8	-14.74	-0.78

Post optimisation results showing the targets are met;

Target channel mass flow deviation: Within +/-5% target

Target maximum velocity magnitude: 0.65m/s meets target

Target maximum pressure drop: 671Pa – meets target

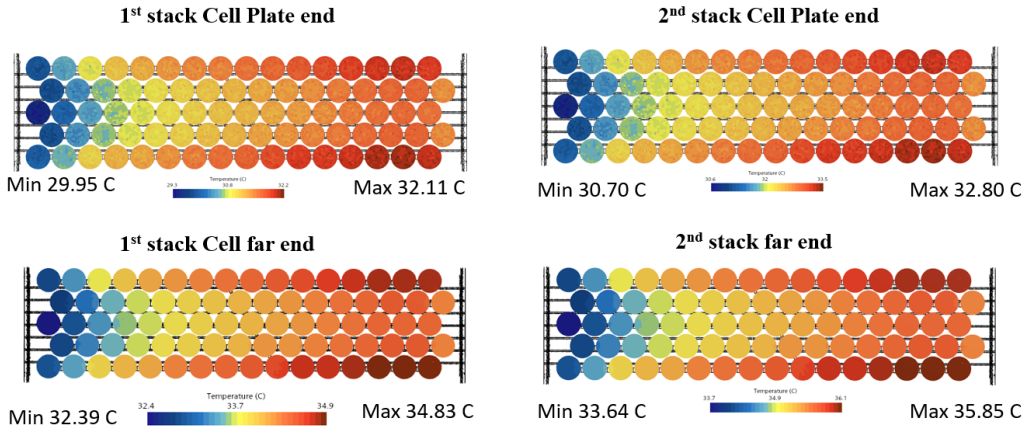


Figure 5.29 Post initial optimisation cell minimum and maximum cell temperature values

Figure 5.29 shows that post initial flow optimization the highest temperature and temperature variation between the cells is at around 35.85-29.95=5.9˚C and is missing our target of maximum 5˚C. The legend advisus us that the main cause of

this is top and bottom rows of the cells lacking contact surface to the cooling plate comparing to the inner battery cell rows .

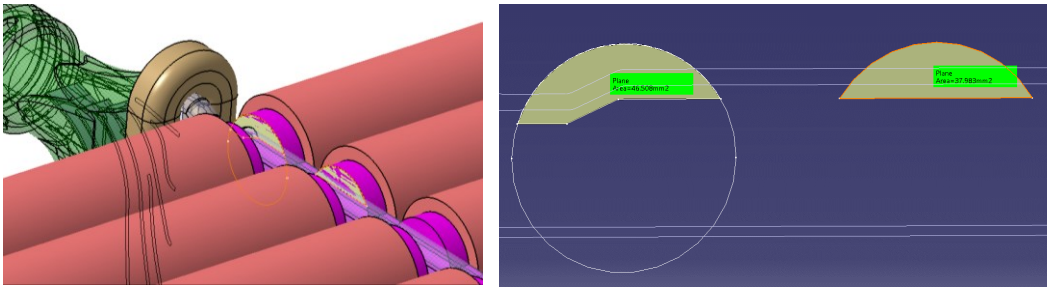


Figure 5.30 Top and bottom cells lacking contact surface to cooling plate

The lack of contact to the cooling plate of the upper and lower battery cells can be observed in figure 5.30. This is causing disadvantage to the discharge of heat from these cells. To resolve this we will modify the deflector to provide proportionally higher mass flow to bottom and top coolant channels. The contact area is ~40/200 smaller with comparison to the middle battery cell rows. Aim is to supply 20% more to the top and bottom channels in comparison to the middle ones. The new target for top and bottom coolant channels is to have 14% flow than balance. And intermediate ones will have 5% less than balance.

5.13 Supplementary Flow Optimisation

Further optimisation has been carried out with deflector iteration number 15. A section view can be seen in figure 5.31.

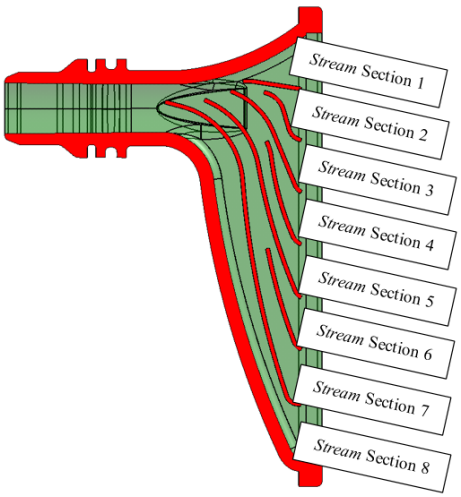


Figure 5.31 Deflector iteration 15 section view

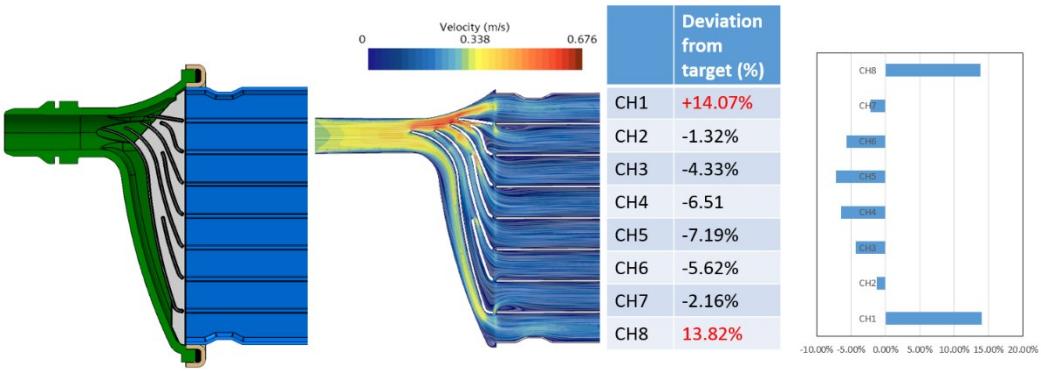


Figure 5.32 Deflector iteration 15 massflow distribution vs target

Coolant flow distribution and coolant massflow deviations per channel post supplemantary optimisation is shown in figure 5.32. Table 5.13 shows the Reynolds number assessment results for the new stream channels created with the deflector iteration number 15. All staying in laminar flow. The pressure drop results an be seen in figure5.33, showing the pressure drop is staying within the target range, below 800Pa

Table 5.13 Reynolds numbers calculated for each stream section channel on supplementary optimisation geometry

	Height	Width	Dh	μ dynamic Vicousity	Max Flow Speed	Reynolds number	Flow Type
	m	m	m	Ns/m^2	m/s	High speed flow	
Section 1	2.02E-03	3.70E-03	2.61E-03	3.84E-03	0.7	507.97	Laminar
Section 2	1.04E-03	3.70E-03	1.62E-03	3.84E-03	0.7	315.60	Laminar
Section 3	2.53E-03	3.70E-03	3.01E-03	3.84E-03	0.7	584.13	Laminar
Section 4	1.40E-03	3.70E-03	2.03E-03	3.84E-03	0.7	394.86	Laminar
Section 5	2.18E-03	3.70E-03	2.74E-03	3.84E-03	0.7	533.28	Laminar
Section 6	1.53E-03	3.70E-03	2.16E-03	3.84E-03	0.7	420.79	Laminar
Section 7	2.69E-03	3.70E-03	3.12E-03	3.84E-03	0.7	605.52	Laminar
Section 8	3.54E-03	3.70E-03	3.62E-03	3.84E-03	0.7	703.31	Laminar

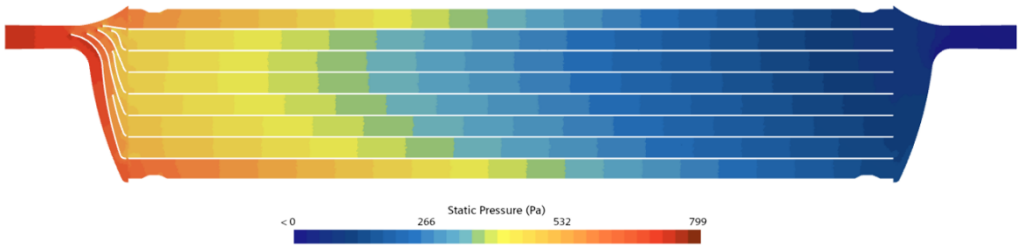


Figure 5.33 Deflector iteration 15 pressure drop

5.14 Supplementary Optimisation Thermal Results

Figur 5.34 shows a legend and a summary of the minimum and maximum temperature readings from the CFD model. Comparison between temperature readings between initial and supplementary flow optimisation studies can be seen in table 5.14. With supplematary flow optimization the highest temperature and temperature variation between the cells is at around 4.9 ˚C and is meeting our target of maximum 5˚C.

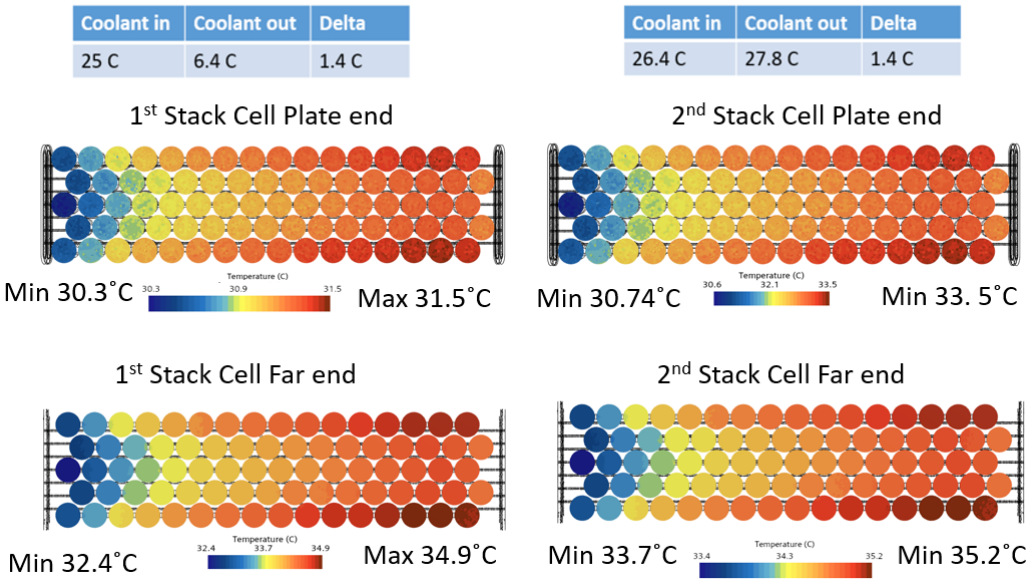


Figure 5.34 Deflector iteration 15 thermal results

Table 5.14 Initial and supplemetary optimisation thermal comparison

	Post Initial optimisation	Post Supplementary optimisation
Temperature at Coldest cell point (˚C)	29.95	30.3
Temperature at hottest cell point (˚C)	35.85	35.2
ΔT (˚C)	5.9	4.9

Design target of not having more than 5C temperature gap between the hottest and coldest points of any cells within the bcattery cell pack has been achieved.

6
MODEL VALIDATION

6.1 Validation Method

Flow optimisation CFD Model correlation to be validated using Bernoulli principle. Venturi tubes for each channel are designed (Figure6.1) and 3D printed then attached to a cut cooling plate for observation of the ΔP values on inlet outlet and each channel. Readings are compared with the CFD model run using same parameters but applied to the venturi geometry.

A separate CFD analyisis is run with the venturi tube geometry to confirm the models correlation, then the readings form the physical test rig are are compared with CFD model analysis results (Figure 6.2).

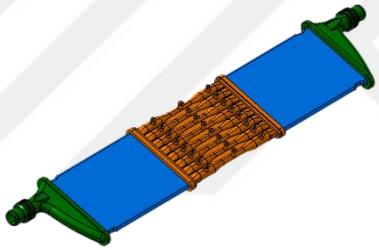


Figure 6.1 3D printed Venturi tube in the middle of the cooling plate

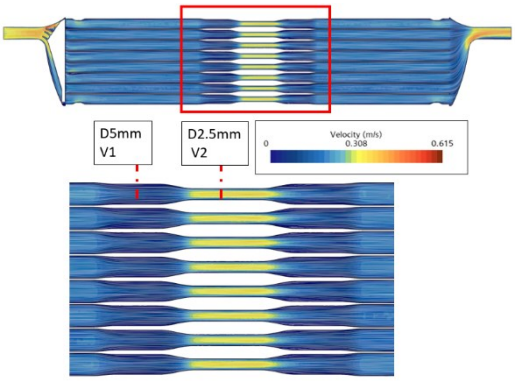


Figure 6.2 CFD Model of the 3D printed Venturi tube for correlation

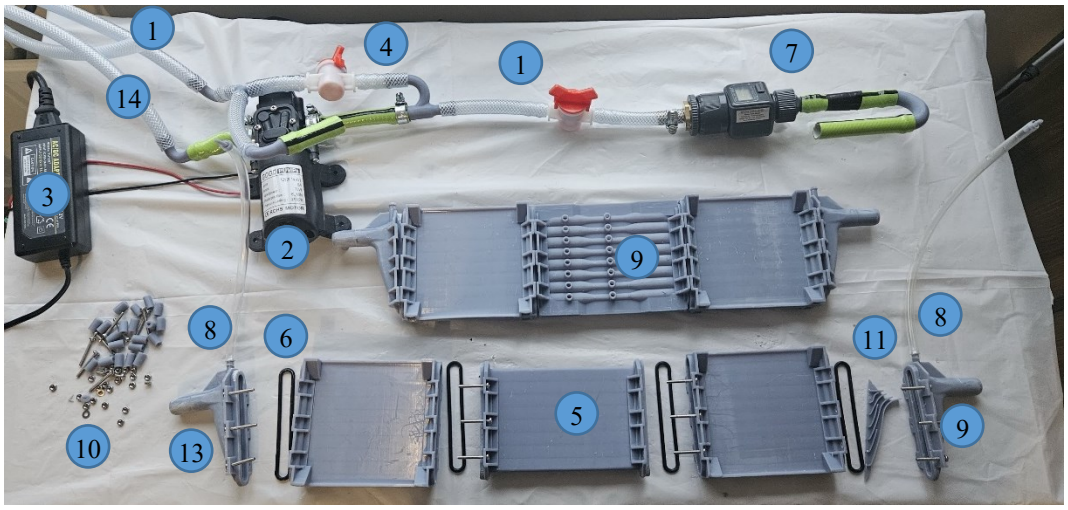


Figure 6.3 Model correlation test rig

Figure 6.3 shows elements of the test rig; 1- Feed line, 2- 12V 0.9Mpa 6L/min pump, 3- 12V Adapter, 4- by pass line and valve, 5- original plate design, 6- sealing rings, 7- flow meter, 8- pressure measure/degas spigots, 9- fluid inlet end tank, 10- fasteners, 11- deflector, 12- venturi plate, 13- fluid out end tank, 14- return line.

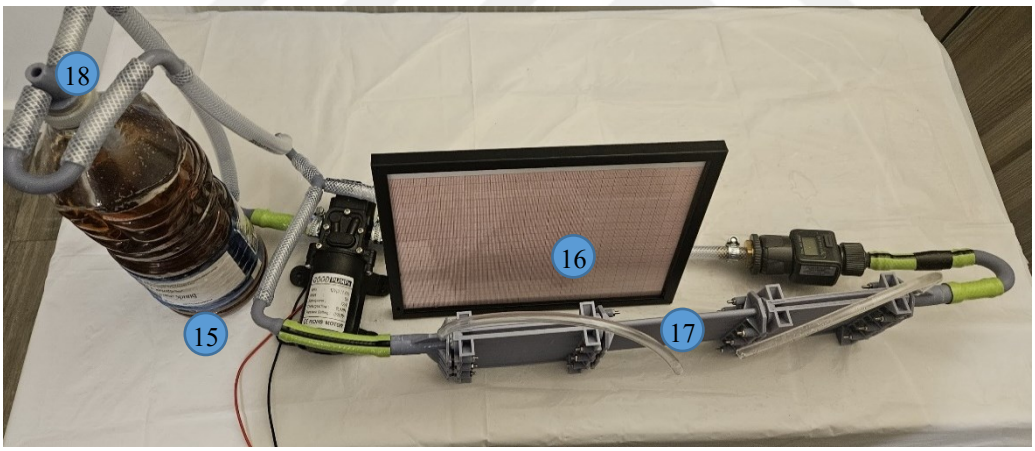


Figure 6.4 Original plate geometry model delta pressure measuring test rig

Figure 6.4 shows components of the test rig; 15- bottle used to store fluid. (It is a closed cup container, filled with water or ethanol mix, based on the test running). It has a degas line inlet spigot. Water is artificaially coloured darker to be help readings on venturi pipes. Coolant mixture is green/yellow colour. 16- Milimetric board for measurement, 17- 3D print of original plate geometry, 18- inlet&outlet degas spigot.

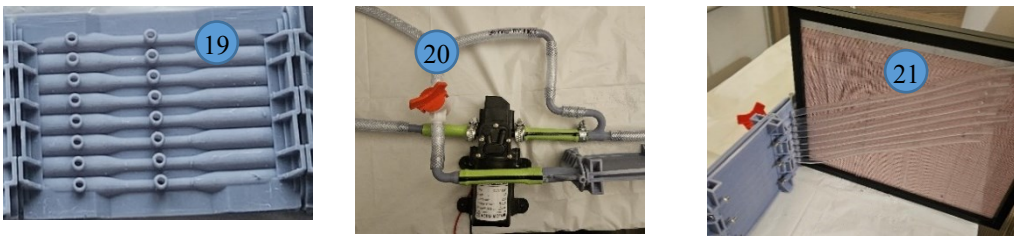


Figure 6.5 Venturi plate geometry model delta pressure measuring test rig

Figure 6.5 shows components of the test rig; 19- Venturi board, 20- back pressure regulator to stabilise the back pressure is added to the test rig upon necessity, 21- venturi pipes to measure fluid pressure in the channels. Figure 5.6 shows positioning the liquid container in a lover height to rduce the back pressure required.



Figure 6.6 Fluid bottle height is lowered to reduce the pressure required due to the height difference on the return line.

6.2 Execution of the Model Correlation Tests

The validation is carried out with two different fluids, water and Ethanol – Water 50/50 coolant mixture. Volumetric flow rate and plate outlet backpressure is adjusted with the valves on feed, return and by pass lines. The system is run until the complete gas leaves the test circuit and flow reches steady state before taking measurements. Fluid tank is lovered to a lower height from the 3D printed plates to reduce the back pressure required to pump fluid up. Following measurements were taken to measure the accuracy of the CFD model.

Water flow measuremets

1. Delta pressure on original plate geometry without deflector

2. Delta pressure on original plate geometry with deflector

3. Static pressure readings on venturi plate geometry without deflector

4. Static pressure readings on venturi plate geometry with deflector

Ethanol based coolant – water 50/50 Mixture measurements

5. Delta pressure on original plate geometry without deflector

6. Delta pressure on original plate geometry with deflector

7. Static pressure readings on venturi plate geometry without deflector

8. Static pressure readings on venturi plate geometry with deflector

Figures 6.7, 6.8, 6.9 and 6.10 in the following pages show photos from the test rig at the moment of a fluent and free from bubbles flow is settled. Two sets of readings have been taken with water as a liquid and 50-50 water – ethanol mixed coolant as liquid. Graph paper is used to read measurements. The ruler is for reference only. The viewing angle and the space between the paper and the ruler (glass and gap in between) are the causes of the misalignment between the ruler and graph paper that can be observed in the pictures. Photo in the figure 6.11 which was shot on a flat surface without any gaps or angles in between, shows how the ruler and the graph line up.

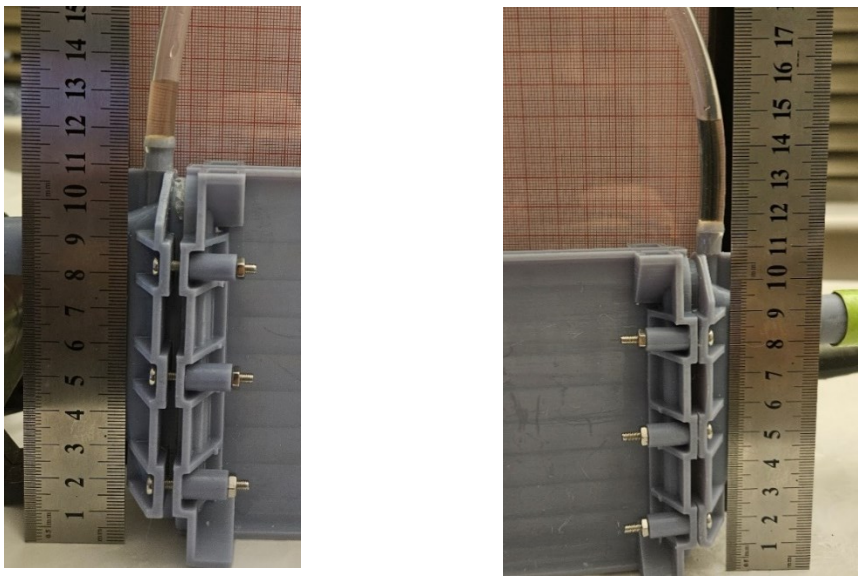


Figure 6.7 Example static pressure measurement from plate outlet an inlet suinf water as liquid

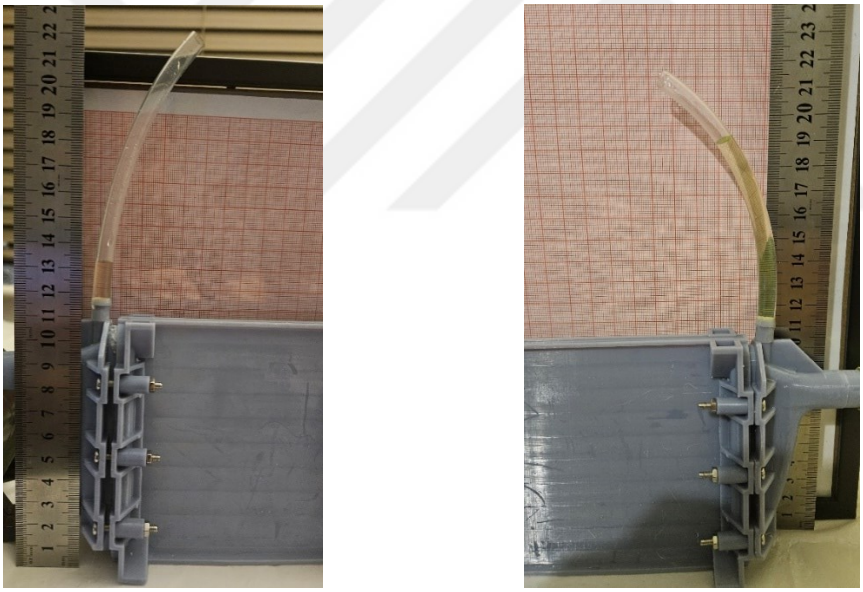


Figure 6.8 Example static pressure measurement from plate outlet an inlet using ethanol coolant mixture as liquid

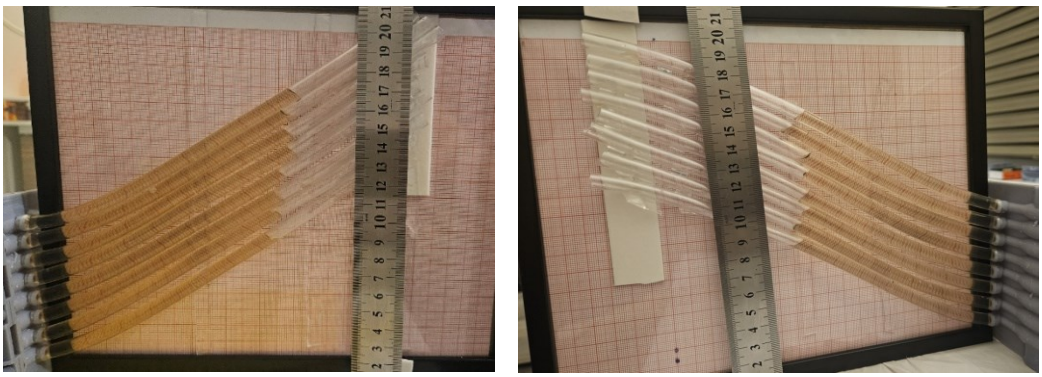


Figure 6.9 Example static pressure measurement from 5mm and 10mm ID tubes using water as liquid

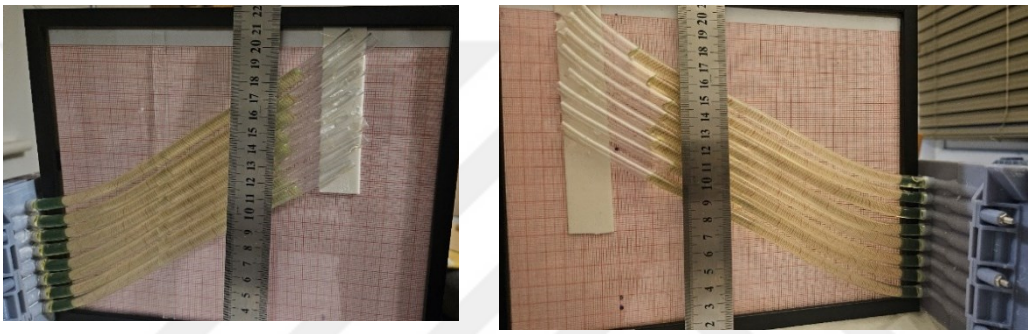


Figure 6.10 Example static pressure measurement from 5mm and 10mm ID tubes using ethanol water mixture as liquid

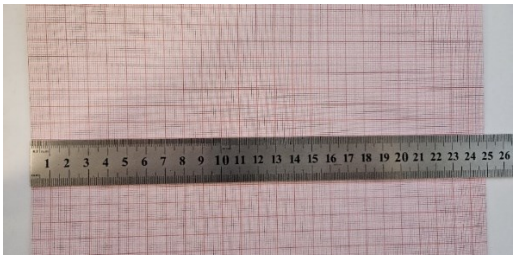


Figure 6.11 Ruler and graph paper alignment

Table 6.1 Comparison of CFD results with physical test measurements

				Delta P	Olet	Delta P CFD	Delta P Measured	Alignment to CFD
				Pa	Pa	Pa	Pa	(%)
Original Geometry	Water	No deflector		207	0	207	206	100
Original Geometry	Water	Deflector 15		305	0	305	284	93
Original Geometry	Coolant	No deflector		550	0	550	540	98
Original Geometry	Coolant	Deflector 15		730	0	730	697	95
	Water	No deflector		Wide_P1	Tight_P2			
Venturi Geometry	INLET	OUTLET		204	0	204	186	91
	CH1			159.6	104.4	55.2	49	89
	CH2			185.2	104.5	80.7	78	97
	CH3			180.9	104.9	76	69	90
	CH4			155.5	102.5	53	49	93
	CH5			143.7	103.5	40.2	39	98
	CH6			145.1	107.7	37.4	39	105
	CH7			148.4	111.9	36.5	39	108
	CH8			150.3	117.9	32.4	29	91
	Water	Deflector 15		Wide_P1	Tight_P2			
Venturi Geometry	INLET	OUTLET		291	0	291	265	91
	CH1			168.9	109.6	59.3	59	99
	CH2			135.3	92.4	42.9	39	91
	CH3			136.3	93.6	42.7	39	92
	CH4			139.5	97.5	42	39	93
	CH5			151.2	105.7	45.5	39	86
	CH6			160.7	113.5	47.2	39	83
	CH7			177.9	124.3	53.6	49	92
	CH8			217.6	145.6	72	69	95
	Coolant	No deflector		Wide_P1	Tight_P2			
Venturi Geometry	INLET	OUTLET		486	0	486	541	111
	CH1			318.0	237.5	80.5	94	116
	CH2			348.2	247.0	101.2	114	113
	CH3			350.3	250.0	100.3	114	114
	CH4			323.5	239.0	84.5	94	111
	CH5			312.2	236.3	75.9	83	110
	CH6			314.6	240.7	73.9	83	113
	CH7			317.7	245.5	72.2	83	115
	CH8			317.0	252.3	64.7	73	113
	Coolant	Deflector 15		Wide_P1	Tight_P2			
Venturi Geometry	INLET	OUTLET		648	0	648	645	99
	CH1			340.0	250.8	89.2	83	93
	CH2			300.5	221.7	78.8	78	99
	CH3			299.4	222.8	76.6	81	106
	CH4			304.7	228.3	76.4	83	109
	CH5			313.3	236.8	76.5	83	109
	CH6			324.6	246.6	78	83	107
	CH7			338.4	258.1	80.3	88	110
	CH8			391.6	297.4	94.2	104	110

Table (6.1) compares the CFD report readings to the physical test conducted with 3D printed prototypes. The table excludes the static pressure occuring at the outlet spigot due to the following bends and height changes. An additional valve is added

after the outlet spigot to regulate the outlet pressure at ~500Pa, so that the water/coolant column can be visible above the spigots.

The CFD model and physical readings are aligned between the ranges from 83% to 116% for whole tests conducted. In a single test configuration the highest variation is on the Venturi-coolant-Deflector15 case with 21%. Considering the noise factors such as temperature, fluid mixture rate, 3D printing geometric tolerance and dffrence in the surface porosity, flow meter's accuracy and low resolution fluid height reading (0-11mm for channel readings and 0-62 mm for plate inlet to outlet readings) these mismatchs are indicating a good alignment between the CFD model and the real life condition.

6.3 Uncertainty Analysis

Since the static pressure is function of density (ρ), height (h), and gravitational acceleration (g), we need to conduct an uncertainty analysis to understand the possible physical measurement/calculation uncertainty. Pressure at a given measurement point is calculated using liquid column height on the venturi tubes.

The formula for that calculation is;

$$P_{fluid} = \rho g h \tag{6.1}$$

Where P is static pressure (Pa),

ρ is density of the coolant (kg/m³)

g is gravitational acceleration (m/s²) and

h is measured liquid height at particular point (m).

The reading tolerances for ρ is 1060 kg/m³ ± 50kg/m³ and for h is 10mm ±0.5mm

The uncertainty can be calculated with the following formula;

$$W_P = \pm\left[\left(\frac{\partial P}{\partial \rho} w_\rho\right)^2 + \left(\frac{\partial P}{\partial h} w_h\right)^2\right]^{\frac{1}{2}} \tag{6.2}$$

$$\frac{\partial P}{\partial \rho} = gh = 9.81 * 0.1 = \frac{0{,}981 m^2}{s^2}$$

$$\frac{\partial P}{\partial h} = g\rho = 9.81 * 1060 \frac{kg}{m^3}$$

$$W_P = \pm \left[\left(ghw_\rho \right)^2 + (g\rho w_h)^2 \right]^{\frac{1}{2}} \quad (6.3)$$

$$W_P = [(9.81 * 0.1 * 50)^2 + (9.81 * 1060 * 0.0005)^2]^{\frac{1}{2}} = \pm 49.32 \text{ Pa}$$

There is an uncertainty of ± 49.32 Pa in the pressure measurements from liquid height column readings.

$$\frac{W_P}{P} = \pm \frac{Wp}{\rho g h} = \frac{49.32}{1060 * 9.81 * 0.1} = \pm 0.47 = \pm 4.7\% \quad (6.4)$$

The discrepancy between CFD results and physical measurements is in the range of -17% and +16%, which is not lower than the uncertainty value, ±4.7%. As it is known, the result of the CFD study cannot be more precise than the uncertainty result. It is understood that the results obtained are consistent.

7
CONCLUSION

It is observed that optimizing the flow deviations reaching 17% to the preferred mass flow alone is not enough to balance the cell temperature variation within the target values. Further optimisations has been required to balance the cooling effect and cover for the lacking contact area on the thermal path of the lower and upper cells. The cells with full contact area to the cooling plate generally manage to stay 1 and 2˚C degrees colder comparing to the battery cells on the lower and upper rows that have less 15% less contact to the cooling plate. Increasing the coolant flow by 20% on top and bottom channels to help battery cells on outer rows resulted in additional homogenisation in steady state temperatures of the battery cells and helped meeting the initial requirement to stay within maxmimum of 5˚C gap between hottest and coldest temperature measurement point.

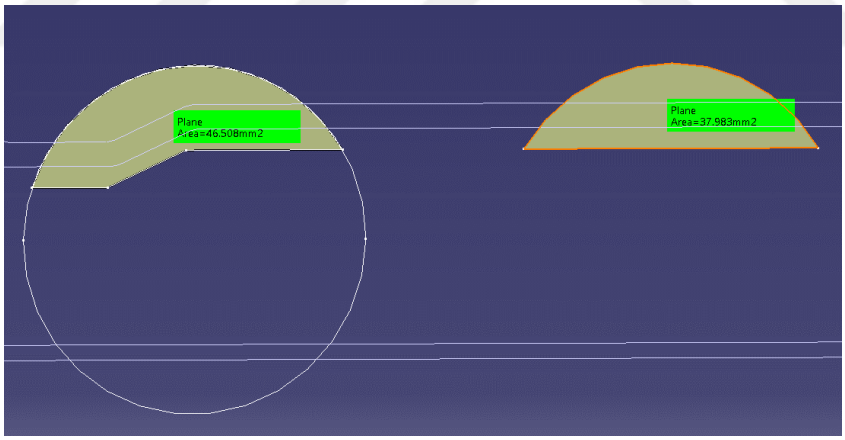


Figure 7.1 Top and bottom cells missing contact area with cooling plate

Figure 7.1 shows the lacking contact area to the cooling plate of the top and bottom battery cell row. To be 40/200 mm^2. Physical correlation activity on the other hand provided confident results about the CFD models accuracy. Despite the numerous noise factors mentioned in the validation section the mismatch between the CFD results and physical readings stayed in reasonable levels proving the CFD model have acceptable fidelity.

Table 7.1 Comparison of the engineering targets and optimisation results

Engineering Target	Target	Status
Max battery cell temperature	40 ˚C	35.2˚C
Flow type	Laminar	Laminar
Pressure drop	Less than 800Pa	735Pa
Coolant flow speed	Les than 0.7m/s	0.676m/s
Max temperature variation	5˚C	4.9˚C

The engineering targets set on the beggining of the study has been met and can be seen summarized in the table 7.1.

REFERENCES

[1] Chunjing Lin, Haoran Wen, Lei Liu, Shiqiang Liu, Tianyi Ma, Bin Fan, Fang Wang, “Heat generation quantification of high-specific-energy 21700 battery cell using average and variable specific heat capacities,” China Automotive Technology and Research Center Co., Ltd. (CATARC), Tianjin, China, Harbin Institute of Technology, Harbin China School of Chemical Engineering and Technology, Tianjin University, China, 2020.

[2] E. Vásquez-Alvarez, F. T. Degasperi, L. G. Morita, M. R. Gongora-Rubio and R. Giudici, “Development Of A Micro-Heat Exchanger With Stacked Plates Using Ltcc Technology,” Universidade de São Paulo, Escola Politécnica, Department of Chemical Engineering, São Paulo, Brazil, Faculdade de Tecnologia de São Paulo, São Paulo - SP, Brazil, Instituto de Pesquisas Tecnológicas, São Paulo - SP, Brazil, 2010.

[3] Ding Zhao, Chao An, Zhiguo Lei, “Liquid cooling plate with drop-shaped deflectors based on Coanda Effect - For Li-ion battery thermal management,” College of Mechanical and Electrical Engineering, Fujian Agriculture and Forestry University, Fuzhou, Fujian, China, 2023.

[4] Ummid Isamiya Shaikh, Dhanapal Kamble and Sandeep Kore, "A Review On Cooling Methods Of Lithium-Ion Battery Pack For Electric Vehicles Applications," Vishwakarma Institute of Information Technology, Maharashtra, India, Pimpri Chinchwad College of Engineering, Maharashtra, India, 2024.

[5] Xu Xiaoming, Jiaqi Fu, Haobin Jiang, Ren He, "Research on the heat dissipation performance of lithium-ion cell with different operating conditions," Jiangsu University, 2017.

[6] Yunus A. Çengel, Afshin J. Ghajar, “Heat and Mass Transfer, Fundementals and Applications,” McGraw-Hill Education, 5th edition, 2015.

[7] Yunus A. Çengel, John M. Cimbala, “Fluid Mechanics, Fundementals and ApplicationsHeat and Mass Transfer, Fundementals and Applications,” McGraw-Hill Education, 3rd edition, 2013.

[8] Kundu P.K. and Cohen I.M, “Fluid Mechanics,” Elsevier Academic Press, 2003.

[9] Siemens, “Simcenter Star CCM+ Tutorial Guide, Star-CCM+ 2310,” 2024.

[10] Thermopedia “Bends, flow and pressure drop in,” (Accessed: January 2024) https://www.thermopedia.com/content/577, 2011.

[11] EngineeringToolbox “Various engineering data and calculation tools” https://www.engineeringtoolbox.com/, (Accessed: January 2024)

PUBLICATIONS FROM THE THESIS

Conference Papers

1. ISPEC 16th INTERNATIONAL CONFERENCE ON ENGINEERING & NATURAL SCIENCES 01-02 June 2024 http://www.ispecongress.org/